1 **In situ structures of periplasmic flagella reveal a distinct cytoplasmic ATPase complex in *Borrelia***

2 ***burgdorferi***

3

4 Zhuan Qin[1, 2]*, Akarsh Manne[3]*, Jiagang Tu[2]*, Zhou Yu[3], Kathryn Lees[3], Aaron Yerke[3], Tao Lin[2],

5 Chunhao Li[4], Steven J. Norris[2], Md A. Motaleb[3#], Jun Liu[1, 2#]

6

7 1   Department of Microbial Pathogenesis & Microbial Sciences Institute, Yale University, New

8 Haven, CT 06519

9 2   Department of Pathology and Laboratory Medicine, McGovern Medical School, Houston, TX

10 77030.

11 3   Department of Microbiology and Immunology, Brody School of Medicine, East Carolina

12 University, Greenville, NC 27834

13 4   Philips Research Institute, School of Dental Medicine, Virginia Commonwealth University,

14 Richmond, VA 23298

15

16

17 * Z. Q., A.M., and J.T. contributed equally to this work.

18

19 # Corresponding authors:

20 jliu@yale.edu (J. L.);

21 motalebm@ecu.edu (M.A.M.)

22

23

24 Running title: *Novel ATPase complex structure in periplasmic flagella*

25

26

26
27 **ABSTRACT**
28

29 Periplasmic flagella are essential for the distinct morphology and motility of spirochetes. A flagella-

30 specific Type III secretion system (fT3SS) composed of a membrane-bound export apparatus and a

31 cytosolic ATPase complex is responsible for the assembly of the periplasmic flagella. Here, we

32 combine cryo-electron tomography and mutagenesis approaches to characterize the fT3SS machine in

33 the Lyme disease spirochete *Borrelia burgdorferi*. We define the fT3SS machine by systematically

34 characterizing mutants lacking key component genes. We discover that a distinct cytosolic ATPase

35 complex is attached to the flagellar C-ring through multiple spoke-like linkers. The ATPase

36 complex not only strengthens structural rigidity of the C-ring, but also undergoes conformational

37 changes in concert with flagellar rotation. Our studies provide structural framework to uncover the

38 unique mechanisms underlying assembly and rotation of the periplasmic flagella and may provide

39 the bases for the development of novel therapeutic strategies against several pathogenic spirochetes.

40

41

2

41
42   **INTRODUCTION**

43   Spirochetes are a group of bacteria responsible for several serious human diseases including

44   Lyme disease (*Borrelia* or *Borreliella* species), syphilis (*Treponema pallidum* subsp. *pallidum*), and

45   leptospirosis (*Leptospira interrogans* and other *Leptospira* species). Spirochetes are easily recognized by

46   their distinctive wave-like or helical morphology and unique form of motility, but remain poorly

47   understood. Their motility is driven by periplasmic flagella, which reside and rotate within the

48   periplasmic space between the outer membrane and the peptidoglycan layer. Recent genetic studies

49   indicate that their unique motility is crucial for host infection and/or bacterial transmission by all

50   pathogenic spirochetes studied to-date (Lambert et al., 2012; Li et al., 2010; Motaleb et al., 2015; Sultan

51   et al., 2013; Sultan et al., 2015; Wunder et al., 2016). Rotation of the periplasmic flagella against the

52   elastic cell body contributes to the distinctive morphology and motility of spirochetes. For example,

53   mutants *B. burgdorferi* that lack their periplasmic flagellar filaments encode by FlaB are non-motile

54   and rod shaped (Charon et al., 2012; Charon et al., 2009; Motaleb et al., 2000; Sultan et al., 2013; Sultan

55   et al., 2015).

56   The periplasmic flagella are different from other bacterial flagella in many aspects. In particular,

57   the spirochetal flagellar motor is significantly larger than the motors from most other bacteria,

58   including those of the model organisms *Escherichia coli* and *Salmonella enterica* (~80 *vs* ~45 nm in

59   diameter). Unique spirochete-associated features include the periplasmic collar, which is prominent

60   in *B. burgdorferi* (Moon et al., 2016) and all other spirochetes characterized to date (Chen et al., 2011;

61   Liu et al., 2010a; Murphy et al., 2006; Raddi et al., 2012). The large spirochetal flagellar motors

62   produce the highest torque (~4000 pN.nm) observed in bacteria (Beeby et al., 2016). In addition,

63   spirochetes have unusual flagellar hooks in which the hook proteins are cross-linked by a covalent

64   bond that is required to transmit the torque from the motor to the filament (Miller et al., 2016). These

65   spirochete-specific features enable the spirochetes to bore through viscous environments in the hosts.

66   The filament is the largest component of the periplasmic flagella; it is often as long as 10 μm.

67   Multiple filaments arising from both poles form flat ribbons that wrap around the cell body in a right-

68   handed fashion (Charon et al., 2009). The assembly of the periplasmic flagella is a finely orchestrated

69   process, which includes the initiation of the motor complex subterminally at the cell poles and the

70   formation of the hook and the filament in the periplasmic space (Zhao et al., 2013). The flagellar-

71   specific type III secretion system (fT3SS) is responsible for the assembly of the periplasmic flagella.

72   Although periplasmic flagella are different in location from the external flagella such as those seen in

73   *E. coli*, the fT3SS is conserved among different bacterial species (Chen et al., 2011; Zhao et al., 2014).

74   Furthermore, the fT3SS is evolutionarily related to the virulence (v)T3SSs that promote bacterial

75   virulence by delivering effector proteins into eukaryotic cells (Diepold and Armitage, 2015; Erhardt et

76   al., 2010). The secretion process of T3SS is energized by proton motive force (PMF) (Erhardt et al.,

77   2014; Minamino and Namba, 2008; Paul et al., 2008) and ATP hydrolysis (Claret et al., 2003; Fan and

78   Macnab, 1996; Imada et al., 2007). However, the mechanisms underlying the secretion process are not

79   well understood at molecular level.

80   The fT3SS consists of a membrane-bound export apparatus and a large cytosolic ATPase

81   complex. Six transmembrane proteins (FlhA, FlhB, FliO, FliP, FliQ, and FliR) are thought to form the

82   export apparatus for substrate secretion. Among the six integral membrane proteins, FlhA is the

83   largest, consisting of an N-terminal domain with eight transmembrane regions (FlhA$_{TM}$) and a C-

84   terminal cytoplasmic domain (FlhA$_C$) (Macnab, 2003; McMurry et al., 2004). FlhA facilitates the

85   translocation of the export substrates into the central channel of the growing flagella (Kihara et al.,

86   2001; Minamino et al., 2010; Zhu et al., 2002). FlhB consists of an N-terminal transmembrane domain

87   (FlhB$_{TM}$) and a C-terminal cytoplasmic domain (FlhB$_C$) (Ferris et al., 2005). FliO, FliP, FliQ and FliR are

88   integral membrane proteins, that are also important for substrate secretion (Erhardt et al., 2010).

89   Three cytoplasmic proteins (FliH, FliI, and FliJ) form the ATPase complex that promotes the

90   export process by binding and delivering substrates to the export apparatus (Fraser et al., 2003;

91   Minamino and Imada, 2015). FliI is an ATPase and shows structural similarity with the α and β

92   subunits of the F_0F_1-ATP synthase (Ibuki et al., 2011). FliI exhibits its full ATPase activity when it self-

93   assembles into a homo-hexamer (Imada et al., 2007; Macnab, 2003). FliH probably acts as a negative

94   regulator of the FliI ATPase, and FliJ has a chaperone-like activity that prevents substrate aggregation

95   (Fraser et al., 2003). FliH, FliI, and FliJ coordinately deliver a chaperone-substrate complex to the

96   export gate by binding to the docking platform of the fT3SS for substrate export (Abrusci et al., 2013).

97   FliH$_2$ binds to FliI ATPase and localizes FliI to the bottom of flagellar motor through the interaction

98   with FliN on the C-ring (Minamino et al., 2009). FlhA is required for stable anchoring of the FliI$_6$ ring

99   to the gate (Bai et al., 2014).

100   Recent cryo-electron tomography (cryo-ET) studies have revealed the overall structures of the

101   fT3SS machine within intact flagellar motors (Abrusci et al., 2013; Chen et al., 2011; Liu et al., 2010a;

102   Liu et al., 2009; McMurry et al., 2006; Raddi et al., 2012; Zhao et al., 2013). However, these studies

103   have yet provided sufficient details to dissect protein-protein interactions at the molecular level. More

104   importantly, the structure and function of each component have not been systematically analyzed in

105   the context of the intact flagellar motor.

106   *B. burgdorferi* is the best-studied spirochete system. Recent breakthroughs in genetic

107   manipulations allow the production of well-defined mutations without imposing any secondary

108   alterations (Moon et al., 2016; Motaleb et al., 2011; Sultan et al., 2015; Zhao et al., 2013). The small cell

109   diameter and the highly ordered array of multiple flagellar motors in *B. burgdorferi* make it an

110   excellent model system for *in situ* structural analysis of the periplasmic flagella by cryo-ET. Our

111   previous structural analysis of wild-type cells and several rod mutants of *B. burgdorferi* not only

112   revealed the sequential assembly of the flagellar rod, hook, and filament, but also showed the intact

113   fT3SS machine within the C-ring and beneath the MS-ring (Zhao et al., 2013). Furthermore, disruption

114   of the *fliH* and *fliI* genes by transposon mutagenesis was found to disrupt the assembly and

115   placement of the cytoplasmic ATPase complex and to greatly inhibit flagellar filament formation,

116   which were largely restored by genetic complementation (Lin et al., 2015). However, structural details

117   of the fT3SS machine and its interactions with other flagellar components remain elusive, likely

118   because of the dynamic nature of the fT3SS machine and the difficulty of symmetry-matching among

119   the flagellar subunits.

120   In this study, we used cryo-ET and sub-tomogram averaging to reveal novel features of the intact

121   fT3SS machine in wild-type (WT) *B. burgdorferi* flagellar motor. We gained an in-depth understanding

122   of the subunit organization and function of the fT3SS machine by systemically characterizing

123   structural changes in several single and multiple deletion variants of the fT3SS in the *B. burgdorferi*

124   flagellar motor. Comparison of these results with recent studies of the T3SSs in external flagella and

125   evolutionarily related bacterial injectisomes provides new insights into these nanomachines that share

5

126 a common evolutionary origin, but are structurally and functionally different (Hu et al., 2017; Hu et

127 al., 2015; Kawamoto et al., 2013; Zhu et al., 2017).

128

129 **RESULTS**

130 *In situ* **analysis of the** *B. burgdorferi* **flagellar motor reveals novel features of the fT3SS machine**

131 Nine conserved proteins of *B. burgdorferi* are believed to form the membrane-bound export

132 apparatus and the cytosolic ATPase complex (Fig. 1), although the exact details remain to be defined.

133 To dissect the molecular architecture of the intact fT3SS machine, we utilized high-throughput cryo-

134 ET and a sophisticated sub-tomogram classification to analyze the *B. burgdorferi* flagellar motor. By

135 analyzing images of over 20,000 motors extracted from the cell poles, we generated an asymmetric

136 reconstruction that not only reveals the previously observed 16-fold symmetry of the collar and stator

137 structures (Liu et al., 2009; Moon et al., 2016; Zhao et al., 2013) but also discloses a spoke-like structure

138 underneath the C- and MS-rings (Fig. 2A-F, Movie S1). The spoke-like densities extend from a

139 hexagonal "hub" to the bottom of the C-ring (Fig. 2A, B, E). Multivariate statistical analysis (Winkler,

140 2007) indicates that there are 23 linkers in most flagellar motors, albeit this number can be varied from

141 21 to 24 in some rare instances (see Fig. S1).

142

143 **The ATPase complex is directly connected with the C-ring**

144 To characterize the 'hub and spoke' structures, we compared the structure of the WT motor with

145 those derived from *fliH* and *fliI* mutants (Lin et al., 2015). In either mutant, the 'hub and spoke'

146 densities are absent, as previously reported, suggesting that they are formed by the FliI/FliH ATPase

147 complex (Lin et al., 2015). The C-ring density in the average structures from those two mutants is

148 indistinct compared to that derived from the WT motor (Fig. 2G). However, classification shows that

149 the C-ring from the WT maintains a round shape, while the C-ring from the *fliH* mutant is often

150 ellipse-shaped (Fig. 2H). Therefore, we propose that the FliI/FliH complex forms a large 'hub and

151 spoke' structure that interconnects with the C-ring and plays an unexpected role in stabilizing this

152 prominent C-ring structure.

153

6

FlhA, FlhB, FliP, FliQ, and FliR are essential for flagellar assembly in *B. burgdorferi*

The large density between the ATPase complex and the MS ring is thought to be the export apparatus. To characterize this density (see Fig. 2A and F), we constructed single Δ*flhA*, Δ*flhB*, Δ*fliP*, Δ*fliQ*, Δ*fliR* mutants, respectively. All five mutants are rod-shaped and non-motile, and they do not form flagellar hook or filament, indicating that FlhA, FlhB, FliP, FliQ, FliR are all essential for flagellar assembly and motility in *B. burgdorferi* (see Fig. S3 for an example). However, the flagellar motors are readily visible at the cell tips of these mutants, largely because of the presence of the periplasmic collar (Moon et al., 2016). The collar is also particularly useful as a reference during the subsequent sub-tomogram averaging. Indeed, sub-tomogram averaging of the Δ*flhA* motors reveals the common feature of the collar, but it also shows that the large, complex density underneath the MS ring is absent (Fig. 3C). Moreover, the cytoplasmic membrane beneath the MS-ring is concave (Fig. 3C), suggesting that reorganization of the membrane components occurred in the absence of FlhA. Moreover, the large donut-shaped density beneath the MS ring is absent in Δ*flhA* (Fig. 3C) comparing with WT (indicated by an arrow in Fig 3F). We thus processed sub-tomogram alignment focusing on the density with WT motors. It turned out that the large donut-shaped density has 9-fold symmetry, and has multiple slim links connecting to MS ring (Fig. 3G, Fig. S2). We speculate the donut shaped density should be FlhAc, as its homolog MxiA has 9-fold symmetry and locates at similar position in injectisome (Abrusci et al., 2013). Similar motor structures were also found in the point mutant *B. burgdorferi flhA*D158E cells that exhibit non-motile phenotype, or the reduced-motility mutant displayed by the *flhA*D158N cells (not shown).

In the Δ*flhB* mutant, both the ATPase complex and the export apparatus are evident (Fig. 3D), suggesting that FlhB does not contribute to the structure or positioning of the ATPase complex or the export apparatus. In contrast, in the Δ*fliP* (Fig. 3E, Fig. S4), Δ*fliQ* and Δ*fliR* mutants (Fig. S5, S6), the membrane underneath the MS-ring has a flat surface, and the FlhA complex appears to be absent or disordered. Therefore, the structures of these mutants are strikingly different from the WT structure (Fig. 3F).

Comparative analysis of the four structures shown in Fig. 3C-F suggests that the cytoplasmic domains of the FlhA complexes form the large torus density and the membrane portions of the FlhA

7

182   complexes are inserted into the cytoplasmic membrane (as proposed in Fig. 3H). It has been recently

183   suggested FliP/Q/R are likely to form the central channel complex (Kuhlen et al., 2018; Ward et al.,

184   2018). Our study provided evidence that the assembly of the FlhA complex depends on the formation

185   of the FliP/Q/R channel. FlhB is not well-defined in our structures, but it is essential for fT3SS

186   function.

187

188   **The FlhA complex stabilizes the ATPase complex**

189   The FliI/FliH ATPase complex appears to be associated with the bottom portion of the C-ring,

190   even in the absence of FlhA. However, the FliI/FliH-associated density in the $\Delta flhA$ mutant is

191   indistinct, indicating that the FlhA complex is involved in stabilization of the ATPase complex under

192   the C-ring (Fig. 3C). In addition, the ATPase complex appears to shift away from the MS-ring,

193   implying that there is an interaction between the FlhA and ATPase complexes. Therefore, we propose

194   that the FlhA complex is not essential for the assembly of the ATPase complex, but it provides a

195   docking site to stabilize the ATPase complex. Our result is consistent with previous study that FlhA is

196   required for stable anchoring the $FliI_6$ ring to the export gate (Bai et al., 2014).

197

198   **FliO has a limited role in the flagellar assembly in *B. burgdorferi***

199   FliO is the less conserved among the membrane proteins of the export apparatus. In fact, *B.*

200   *burgdorferi* FliO and its *Salmonella* homolog have very weak sequence identify (13%; Table S1). We

201   generated a $\Delta fliO$ mutant, which is less motile than the WT cells. However, cryo-ET reconstructions

202   revealed that both the flagellar motor and filaments are present in the $\Delta fliO$ mutant (Fig. 4A, F).

203   Furthermore, the flagellar motor and the fT3SS machine in the $\Delta fliO$ mutant (Fig. 4C) are similar to

204   those in WT, suggesting that FliO is relatively less impo rtant for the formation of the fT3SS and the

205   assembly of the flagellar rod, hook and filament in *B. burgdorferi*.

206

207   **The export apparatus has a profound impact on flagellar motor formation in *B. burgdorferi***

208   To understand the overall contribution of the membrane-bound export apparatus proteins to the

209   structure and assembly of the flagellar motor, we generated a quintuple $\Delta fliP$-$flhA$ mutant by deleting

8

210   *fliP, fliQ, fliR, flhB* and *flhA* genes using the Cre-LoxP method (Bestor et al., 2010). As expected, the

211   Δ*fliP-flhA* mutant is also rod-shaped and non-motile. Cryo-ET reconstruction of the mutant shows few

212   motors on the cell tip (Fig. 4B). The average structure of the quintuple-mutant motor (Fig. 4D) is

213   similar to that of the Δ*fliQ* motor (Fig. 4C), although the resolution of the image is relatively poor

214   because fewer motors were available for sub-tomogram averaging. Importantly, the ATPase complex

215   (indicated by orange arrow in Fig. 4D) remains in a similar location as in the Δ*fliQ* or Δ*flhA* motors,

216   supporting the notion that the export apparatus is dispensable for the formation of the ATPase

217   complex. However, absence of the export apparatus proteins has a significant impact on motor

218   formation, as the number of motors per cell tip is highly variable in the mutants of the export

219   apparatus (Fig. 4F). The number of the flagellar motors at each cell tip of the Δ*flhA* mutant is

220   comparable to that of WT (Fig. 4F), suggesting that FlhA does not have a significant effect on motor

221   formation in *B. burgdorferi.* In contrast, the number of the motors in the Δ*flhB* mutant is significantly

222   lower than in WT cells and the Δ*flhA* mutant. These results indicate that FlhB is important for the

223   formation of the motor in *B. burgdorferi* (Fig. 4F), although some motors can still be assembled in the

224   absence of FlhB, FliO, FliP, FliQ, or FliR (Fig. 4F). The impact of the export apparatus proteins on

225   motor formation seems to be cumulative, as demonstrated by the significant decrease in the number

226   of the flagellar motors detected in the quintuple Δ*fliP-flhA* mutant (Fig. 4F). Out of 342 cryo-ET

227   reconstructions from the quintuple mutant, we only identified 54 motors, indicating that the flagellar

228   motors assemble at a very low frequency in the absence of the major membrane proteins (Fig. 4F).

229   Our results are consistent with a model in which there is substantial coordination between the

230   assembly of the MS ring and the export apparatus during the initiation of flagellar assembly (Bai et

231   al., 2014).

232

233   **Molecular architecture of the fT3SS machine in *B. burgdorferi***

234   To better understand the interactions among the fT3SS components in the intact *B. burgdorferi*

235   flagellar motor, we constructed a model of the fT3SS machine and its surrounding C-ring complex

236   based on the available homologous structures. We first built the model of the $FlhA_C$ nonameric ring

237   based on the homologous structures from other bacteria (Abrusci et al., 2013; Saijo-Hamano et al.,

238   2010) (Fig. 5). The entire ring fits well into the torus-like density (Fig. 5B, C), suggesting that the FlhA

239   complexes also form a nonameric ring in *B. burgdorferi.* Three subdomains (SD1, SD3 and SD4) of

240   FlhA$_C$ are located inside the nonameric FlhA$_C$ ring, whereas the SD2 domain is located outside of the

241   ring (Fig. S7). The distance between the FlhA$_C$ ring and the cytoplasmic membrane is about 6 nm. The

242   FlhA$_C$ is linked to the FlhA trans-membrane domain embedded in the cytoplasmic membrane under

243   the MS-ring. The central channel of the export apparatus appears to be aligned with the central axis of

244   the MS-ring and the ATPase complex (Fig. 5D).

245   The ATPase complex can be divided into two major components: a large central hub, and 23

246   spoke-like linkers extending to the C-ring (Fig. 5). The ATPase complex was originally proposed to

247   form a hexamer (Claret et al., 2003; Fan and Macnab, 1996; Imada et al., 2007) and is part of the

248   density beneath the FlhA$_C$ ring, as suggested by analysis of a Δ*fliI* mutant in *Campylobacter jejuni*

249   (Chen et al., 2011) and in *B. burgdorferi* (Lin et al., 2015). FliI, FliH, and FliJ are known to form a large

250   complex that delivers the chaperone-substrate complex to the export gate (Fraser et al., 2003;

251   Minamino and Macnab, 2000). *B. burgdorferi* contains the homologs of these proteins (Fig. S8).

252   Therefore, we postulate that the hexametric density is composed mainly of the FliI/FliJ complex.

253   Based on its similarity with a portion of the F$_0$F$_1$-ATPase, the FliI/FliJ complex was modeled by

254   aligning the monomer structures of *Salmonella* FliI and FliJ to the α$_3$β$_3$ and γ parts of F$_0$F$_1$-ATPase,

255   respectively (Ibuki et al., 2011; Imada et al., 2007). The pseudo-atomic structure of FliI/FliJ fits well

256   into the spherical density (Fig. 5C). The density of FliJ is not well resolved in our maps, probably

257   because of its small size or dynamic nature (Ibuki et al., 2011). The N- and C-termini of FliJ insert into

258   the middle of six FliI subunits, while the middle part of FliJ inserts into the nonameric FlhA$_C$ ring (Fig.

259   5C).

260   A FliH dimer is known to form a stable complex with the FliI ATPase (Minamino and Macnab,

261   2000). The C- terminal domain of FliH is involved in binding to FliI, while a small central region of

262   FliH is essential for formation of the FliH dimer (Gonzalez-Pedrajo et al., 2002). The N-terminal

263   domain is important for FliH-FliN interactions (Minamino et al., 2009). The C-terminal domain of the

264   FliH dimer interacts with the N-terminal domain of FliI, while the N-terminal domain of the FliH

265   dimer can extend toward FliN at the bottom of the C-ring. We propose that 3 or 4 FliH dimers form

10

266 each of the hub-like structures. We speculate that one FliH dimer directly binds to one FliI monomer,

267 while others bind to the adjacent FliH dimer in a parallel fashion. In total, there are six bundles of

268 FliH dimers, each of which interacts with one FliI monomer (Fig. 5E, F). The N-terminal domain of the

269 FliH dimer binds to FliN at the bottom of the C-ring (Fig. 5E), and the hydrophobic patch (L85, T110,

270 V128, V130, F135) at the C-terminus of FliN has been reported to interact with FliH (Minamino et al.,

271 2009). The atomic models of FliG, FliM and FliN (Vartanian et al., 2012), which were docked into the

272 C-ring, reveal that these hydrophobic residues of FliN (labeled red in Fig. 5D, Movie S2) are near the

273 tip of the FliH linker.

274

275 **Variable conformations of the ATPase complex and the C-ring**

276 The C-ring is thought to rotate together with the MS ring and the flagellar filament, although the

277 rotation of the C-ring has not been directly visualized. The detail of our *in situ* structures is not

278 sufficient to visualize the C-ring and its rotation. However, we are able to resolve multiple FliH

279 linkers between the ATPase complex and the C-ring. To our surprise, classification of the WT motors

280 resolved multiple conformations, in which the ATPase complex apparently adopts different

281 orientations with respect to the collar and the stator (Fig. 6). Specifically, in the four classes shown in

282 Fig. 6, the collar and stator are in a similar orientation, however, the ATPase complexes in classes 03,

283 05, 08 rotate about 7°, 13°, 20° from class 00, respectively. As the overall model of the C-ring and the

284 ATPase complex fits well into the class averages, we propose that the C-ring and the ATPase can

285 rotate as a large, rigid body (Movie S3).

286

287 **DISCUSSION**

288

289 T3SSs in bacterial flagella and injectisomes are highly conserved. The flagella are elaborate self-

290 assembling machines that serve as the main organelles for bacterial motility. The injectisomes are

291 specialized nanomachines deployed by many important human pathogens such as *Salmonella* spp.,

292 *Shigella* spp. and *Pseudomonas* to deliver virulence effectors into eukaryotic cells. Our previous studies

293 revealed key intermediates of fT3SS-mediated assembly in *B. burgdorferi* (Zhao et al., 2013) and overall

11

294   architectures of the vT3SS machines in *Shigella* and *Salmonella* (Hu et al., 2017; Hu et al., 2015). Here

295   we focus on the structure and function of the fT3SS machine in periplasmic flagella by systematically

296   analyzing mutants lacking key fT3SS components and comparing them to the vT3SS machines (Fig.

297   7). The overall organization of the fT3SS machine in the *B. burgdorferi* periplasmic flagella shares

298   many similar features observed with the fT3SS machine in the *E. coli* external flagella (Zhu et al., 2017)

299   and the vT3SS machines in *Shigella* and *Salmonella* (Hu et al., 2017; Hu et al., 2015; Kawamoto et al.,

300   2013). However, there are considerable differences between the fT3SS and vT3SS.

301   Five conserved membrane proteins (FlhA, FlhB, FliP, FliQ, and FliR) form the export apparatus

302   beneath the MS-ring in *B. burgdorferi*. They are essential for the export of flagellar proteins and for

303   motility. FliP, FliQ, and FliR likely form an export gate in the cytoplasmic membrane. FlhA forms a

304   nonameric ring complex, which provides a docking site for the ATPase complex and substrates. The

305   overall structure of the export apparatus in the *B. burgdorferi* flagellar motor is similar to that in the

306   *Salmonella* injectisome (Fig. 7) and external flagella. Presumably, similar mechanisms are utilized for

307   substrate export.

308   The ATPase complex of the *B. burgdorferi* periplasmic flagella is quite different from that in the

309   *Salmonella* injectisome (Fig. 7) and the *E. coli*/*Salmonella* external flagellum (Kawamoto et al., 2013;

310   Zhu et al., 2017). The ATPase complex is surrounded by a large continuous C-ring of the *B. burgdorferi*

311   flagellar motor, while it is linked to six "pods" in the *Salmonella* injectisome (Compare Fig. 7E, F with

312   G, H). In particular, we observed spoke-like linkers between the ATPase and the C-ring for the first

313   time in any bacterium, as they are not observed in the recent structures from the external flagella

314   (Kawamoto et al., 2013; Zhu et al., 2017). Surprisingly, there are about 23 linkers (Fig. 7E, F). They are

315   considerably longer (6 nm vs. 3 nm) in the fT3SS machine than in the vT3SS machine, mainly because

316   the C-ring is much larger than the pod array (62 nm vs. 36nm in diameter) (Fig. 7). Previous studies

317   provided evidence that OrgB (a FliH homolog) forms the spoke-like structure and interacts with the

318   ATPase complex and SpaO (a FliN homolog) of the vT3SS machine (Hu et al., 2017). In the *B.*

319   *burgdorferi* flagellar motor, the linker between the ATPase and C-ring is likely formed by multiple

320   FliH molecules. Consistent with the longer linker region, FliH of *B. burgdorferi* is significantly larger

321   (305 residues) than its homolog OrgB (170 residues). Thus, the ATPase complex not only provides a

322   large docking platform for substrates recruitment and secretion, but also supports the integrity of the

323   C-ring, which undergoes rotation and switches between clockwise and counterclockwise rotation.

324   We observed many different orientations of the ATPase complex relative to the periplasmic

325   structures of the motor, suggesting that the C-ring and the ATPase complex rotate together beneath

326   the MS-ring. The rotation of the C-ring is driven by sixteen stators that surround the C-ring and a

327   spirochete-specific periplasmic collar (Moon et al., 2016). In contrast, the pods found in *Salmonella*

328   injectisomes do not appear to rotate, although OrgB and SpaO likely undergo high turnover with a

329   cytoplasmic pool. These key differences between the fT3SS and vT3SS underline the distinct

330   mechanisms involved in the assembly and function of flagella and injectisomes.

331   The assembly of the flagellum can be divided into two distinct processes. The first stage includes

332   the formation of the MS-ring, C-ring, export apparatus, and the stator. The second stage, which

333   includes the assembly of the rod, hook, and filament, is mediated by the fT3SS. It is generally thought

334   that the MS-ring is the first unit assembled and is central to flagellar assembly and function (Kubori et

335   al., 1992). Recently, fluorescence microscopy was used to investigate dynamic protein exchange in the

336   assembled *E. coli* motor structure. This study suggested that flagellar assembly is initiated by

337   oligomerization of the export protein FlhA, which is followed by the recruitment of the MS-ring

338   protein FliF (Li and Sourjik, 2011). In another study, FlhA localization in *S. enterica* required FliF, FliG,

339   FliO, FliP, FliQ and FliR, suggesting that FlhA assembles into the export gate along with other

340   membrane components in a coordinated manner during the MS-ring formation (Bai et al., 2014). In *B.*

341   *burgdorferi*, FlhA plays little role in initiation of motor formation, because deletion of *flhA* has no

342   impact on the number of motors per cell tip (Fig. 4F). In contrast, other membrane export proteins

343   (FliP, FliQ, FliR, and FlhB) have considerable impact on motor formation. Even in the absence of FliP,

344   FliQ, FliR, FlhA and FlhB, motor assembly still occurs with very low efficiency. Taken together, our

345   results imply that most export proteins are involved in the coordinated assembly of the MS-ring and

346   export apparatus, whereas FlhA is not critical in this process, at least, in *B. burgdorferi*. Interestingly,

347   similar results were obtained in the *Salmonella* injectisome (Wagner et al., 2010), suggesting that

348   coordination in the assembly of the basal body and export apparatus might be shared by flagella and

349   injectisomes.

13

350 In conclusion, our study reveals unprecedented details about the fT3SS machine in the Lyme

351 disease spirochete *B. burgdorferi*. We systematically characterize the fT3SS machine, map the key

352 components, and document their roles in flagellar structure and function. We present the first

353 structural evidence that the distinct ATPase complex of the fT3SS machine is attached to the flagellar

354 C-ring through multiple spoke-like linkers comprised of FliH. The novel architecture not only

355 strengthens the C-ring, but also enables an optimal translocation of substrates through the ATPase

356 complex and the export apparatus. Remarkably, the ATPase complex together with the C-ring can

357 adopt variable orientations, implying that the fT3SS machine undergoes rotation in concert with the

358 flagellar C-ring. Therefore, our studies not only provide a structural framework for a better

359 understanding of the fT3SSs, but also underscore the striking differences between flagella and their

360 evolutionally related bacterial injectisomes.

361

14

368   **EXPERIMENTAL PROCEDURES**

369   **Bacterial strains and growth conditions.** High-passage *Borrelia burgdorferi* strain B31A (WT) and

370   its isogenic mutants (Table S2) were grown in BSK-II liquid medium supplemented with 6% rabbit

371   serum or on semi-solid agar plates at 35°C in the presence of 2.5% carbon dioxide as previously

372   described (52, 53).

373   **Construction of deletion mutants of *fliP*, *fliQ*, *fliR*, *flhA*, *flhB*, and *FliO*.** All mutants studied in

374   this communication were constructed at East Carolina University. Single mutants were constructed

375   using a gene inactivation methodology that creates deletion mutants without imposing any polar

376   effects (Motaleb et al., 2011). The *fliP* gene (gene locus *BB0275*; a 765 bp gene) was inactivated by

377   replacing *fliP* with the *aadA* coding sequence by using overlapping PCR, as schematically shown in

378   Figure S10. PCR was used to amplify three regions of DNA in three steps. In step one, each DNA

379   region was amplified separately by using PCR pairs P1-P2 (5′-upstream *fliP*, 3′-upstream *fliP*), P3-P4

380   (*aadA* coding sequence of streptomycin resistance gene), and P5-P6 (5′-downstream *fliP*, 3′-

381   downstream *fliP*). Primers P2, P3, P4, and P5 (Table S3) contain several overlapping base pairs, as

382   indicated by different colors in Figure S10. In step two, a PCR product was obtained by using primers

383   P1 and P4 and the purified DNA products for upstream *fliP* and *aadA* as templates. In step three, the

384   final PCR product was obtained by using primers P1 and P6, and the purified DNA products of

385   upstream *fliP-aadA* and downstream *fliP* as a template to amplify the upstream *fliP-aadA*-downstream

386   *fliP* DNA construct. The final PCR product yielded a 2,462-bp product that was gel purified and

387   cloned into the pGEM-T Easy vector (Promega Inc.), and then confirmed by PCR and restriction

388   mapping. PCR-amplified DNA was electroporated into B31A competent cells and plated in BSK-II

389   medium containing 100 µg/ml streptomycin (Motaleb et al., 2007). Construction of the *fliQ*, *fliR*, *flhB*,

390   and *flhA* mutants were similarly achieved. Construction of the *FliO* mutant was achieved by replacing

391   the respectable gene with the *aph1* coding sequence for kanamycin resistance, as described above.

392   Resistant clones were analyzed by PCR for the confirmation of homologous recombination (Figure

393   S11). Primers used in creating these mutants are listed in Table S3.

394   **Construction of point mutants *flhA* D158E and *flhA* D158N in *B. burgdorferi*.** Wild type *B.*

395   *burgdorferi flgB* operon contains 26 genes including the target *flhA* (Fig. S10B, top panel), which is

15

396 transcribed by σ⁷⁰. The point mutants were created as follows. Using WT *B. burgdorferi* B31A cells

397 DNA as the template, the left arm (2094 bp of *flhA*) and right arm (1060 bp downstream of *flhA*) were

398 PCR amplified. Using overlapping PCR, a previously described promoter-less kanamycin cassette (*Pl-*

399 *Kan;* 846 bp) was inserted between the left arm and right arm, as depicted in Figure S10B, and

400 subsequently cloned into pGEM-T Easy vector yielding pGEM-T Easy::*flhA-Pl-Kan.* Using

401 pGEMTeasy::*flhA-Pl-Kan* as the template, point mutations D158E (GAT to GAA) and D158N (GAT to

402 AAT) were made by QuikChange II Site-Directed Mutagenesis Kit (Agilent Technologies Inc.), yilding

403 pGEM-T Easy::*flhA*D158E-*Pl-Kan* and pGEM-T Easy::*flhA*D158N-*Pl-Kan,* respectively. The linearized

404 DNA were then electroporated separately into the competent *B. burgdorferi* B31A cells as described

405 above, and transformants were selected with 200 µg/ml Kanamycin. The antibiotic resistant colonies

406 were sequenced to confirm the point mutations.

407 **Construction of a quintuple mutant *ΔfliP-flhA*.** Deletion of the *fliP, fliQ, fliR, flhB, and flhA* genes

408 was achieved by utilizing the Cre-*lox* recombination system (Bestor et al., 2010) (Figure S12). Briefly,

409 *LoxP* sites were introduced into *fliP* and *flhA* genes in the same orientation and chromosome causing

410 the deletion of the sequence containing genes *fliP, fliQ, fliR, flhB,* and *flhA. LoxP* sites were introduced

411 by PCR amplifying *fliP* and *flhA,* containing a single HindIII site, using PCR primer pairs P31-P32 and

412 P33-P34 (Table S3). The resultant PCR products were gel purified and cloned into the pGEM-T Easy

413 vector (Promega). A HindIII restriction site was engineered flanking the *loxP* site with streptomycin

414 resistance (pABA07) by PCR primer pairs P35-36 and cloned into the pGEM-T Easy vector. The *loxP*

415 site with streptomycin resistance cassette in pGEM-T Easy and *loxP* site with kanamycin resistance

416 cassette (pABA14) were digested with HindIII and cloned into plasmids containing the *fliP* and *flhA*

417 genes in pGEM-T Easy, respectively, which were also digested with HindIII, to create the *loxP*

418 insertion mutant vectors. The integrity of the *loxP* insertion mutant vectors and orientation of the *loxP*

419 sites were confirmed by PCR and restriction mapping (Figure S11).

420 **Determination of polar effect on downstream gene expression.** Our novel gene inactivation

421 system does not impose any polar effects, as we have confirmed and verified previously (Motaleb et

422 al., 2011; Zhao et al., 2013). However, we still determined the effect of a deletion mutant on the

423 expression of the downstream genes using qRT-PCR as described previously (Sze et al., 2013). Total

16

424 RNA was extracted from exponentially-grown *B. burgdorferi* (10 ml) cells by using Direct-zol™ RNA

425 MiniPrep Kit (Zymo Research). To ensure that the samples were free of contaminating genomic DNA,

426 the RNA preparation was digested with Turbo DNase I (Ambion) overnight. The concentration and

427 purity of each RNA sample were measured via spectrophotometry (ND-1000 spectrophotometer;

428 NanoDrop Technologies, Inc., Wilmington, DE) and were also assessed by gel electrophoresis.

429 Samples were checked for contamination of genomic DNA by PCR, using *B. burgdorferi* enolase

430 primers. First-strand cDNA was prepared by using AffinityScript cDNA Synthesis Kit (Agilent)

431 according to the manufacturer's instructions. The resulting cDNA was amplified using a CFX96 Real-

432 Time System (Bio-Rad), with a final reaction volume of 25 μl that contained 10 ng of cDNA, Power

433 SYBR® Green PCR Master Mix (Life Technologies), and *B. burgdorferi* gene-specific primers. *B.*

434 *burgdorferi* enolase was used as an internal control. Real-time PCRs were carried out in triplicate, with

435 consistent results (Figure S13, S14).

436 **Dark-field Microscopy to determine motility and bacterial morphology**. Live *B. burgdorferi* cells

437 were observed under a dark-field microscope (Zeiss Axio Imager. M1) connected to an AxioCam

438 digital camera. Exponentially growing cells were examined for their shape and motility. Almost all

439 mutants were non-motile and rod-shaped (see Fig. S3 as an example).

440 **Frozen-hydrated EM sample preparation.** The frozen-hydrated specimens were prepared as

441 previously described (Liu et al., 2009). Briefly, *B. burgdorferi* culture was centrifuged at 5,000 × g for 5

442 minutes. The pellet was suspended with 1.0 ml PBS. The cells were centrifuged again and suspended

443 in 50~80 μl PBS. The cultures were mixed with 10 nm colloidal gold and were then deposited onto

444 freshly glow-discharged, holey carbon grids for 1 min. Grids were blotted with filter paper and then

445 rapidly frozen in liquid ethane, using a homemade gravity-driven plunger apparatus.

446 **Cryo-electron tomography.** Frozen-hydrated specimens were imaged at -170 °C using a Polara

447 G2 electron microscope (FEI) equipped with a field emission gun and a 16 megapixel CCD camera

448 (TVIPS). The microscope was operated at 300 kV with a magnification of 31,000 ×, resulting in an

449 effective pixel size of 5.7 Å after 2×2 binning. Using the FEI "batch tomography" program, low-dose,

450 single-axis tilt series were collected from each cell at -6 to -8 μm defocus with a cumulative dose of

451 ~100 e⁻/Å² distributed over 87 images and covering an angular range of -64° to +64°, with an angular

17

452   increment of 1.5°. SerialEM was recently used to collect tilt series from WT cells at a Gatan K2 Summit

453   direct detector device (DDD) with dose fractionation mode. The microscope was operated at a

454   magnification of 9,400 ×, resulting in an effective pixel size of 4.45 Å without binning and a

455   cumulative dose of ~60 e⁻/Å² distributed over 61 stacks. Each stack contains 8 images. We developed

456   Tomoauto (a wrapper library) to facilitate the automation of cryo-ET data processing (Hu et al., 2015).

457   The main executable encompasses: drift correction of dose-fractionated data using motioncorr (Li et

458   al., 2013) and the assembly of corrected sums into tilt-series; alignment of tilt-series by IMOD (Kremer

459   et al., 1996); reconstruction of tilt-series into tomograms by TOMO3D (Agulleiro and Fernandez,

460   2011).

461   **3-D image processing and sub-tomogram averaging.** In total, 2,846 tomographic reconstructions

462   of Δ*flhA,* Δ*flhB,* Δ*FliO,* Δ*fliP,* Δ*fliQ,* Δ*fliR,* Δ*fliP-flhA* and WT cells were generated and 12,658 flagellar

463   motor sub-tomograms (256×256×256 voxels) were extracted (Table S4). The sub-tomogram analysis

464   was utilized as previously described (Liu et al., 2009; Zhao et al., 2013). Briefly, the initial orientation

465   of each motor was estimated by the center coordinates of the flagellar C-ring and the collar, thereby

466   providing two of the three Euler angles. To accelerate image analysis, 4×4×4 binned sub-tomograms

467   (64×64×64 voxels) were used for initial alignment. Then, the original sub-tomograms (256×256×256

468   voxels) were utilized for further image analysis. Multivariate statistical analysis and hierarchical

469   ascendant classification were then applied to analyze the intact motor *(Liu et al., 2010b; Winkler, 2007;*

470   *Winkler et al., 2009).* Relevant voxels of the aligned sub-volumes were selected by specifying a binary

471   mask of the motor. Class averages were computed in Fourier space, so the missing wedge problem of

472   tomography was minimized. All class averages were further aligned with each other to minimize

473   differences in motor orientation. Because of the predominant 16-fold-symmetric feature of the

474   flagellar motor, the structure of the T3S machine is not well resolved. A novel procedure was

475   developed in which specific substructures of interest are classified and aligned without applying

476   rotational symmetry. Specifically, classification focusing on the export apparatus revealed significant

477   details in its overall structure and interaction with the C-ring. The cytoplasmic portion of the export

478   apparatus complex shows evident features in 6-fold symmetry, while the periplasmic features

479   maintain in 16-fold symmetry (Fig. 2G).

480

481   The average structure of the spoke from WT was generated by aligning the ATPase region and

482   classification on the spoke region using eigenimages 1 to 18 (See Fig. S1 A). The first 40 eigenimages

483   of the data set of ~30,000 sub-tomograms show different symmetry of the spoke region (See Fig. S1B).

484   Eigenimages 01 and 02 exhibit 23-fold symmetry. Eigenimages 04 and 07 exhibit 22-fold symmetry.

485   Eigenimage 08 and 09 exhibit 21-fold symmetry. Eigenimage 10 and 11 exhibit 24-fold symmetry. The

486   eigenimages were ranked by the highest values, which accounts for larger percentage of the total

487   variance of the data set.

488   To obtain the symmetry mismatching structures in Fig 6. and compare the rotation angles, the

489   class averages shows the spoke-like links were selected and aligned based on the region of the C-ring

490   and the ATPase with links. Then they were classified on the collar and stator region. The new class

491   averages that show the symmetry of the collar and stator were selected and aligned by the collar and

492   stator region with spin alignment only. The spin rotation angle were recorded and compared.

493   **3-D visualization and modeling**. UCSF Chimera (Pettersen et al., 2004) was used for 3-D

494   visualization of flagellar motors. Using "match maker" in UCSF Chimera, we built the nonameric ring

495   model of FlhA$_C$ based on the homologue MxiA$_C$ (PDB: 4A5P) from *S. flexneri* (Abrusci et al., 2012). The

496   model of the FliI-FliJ complex was built by aligning the hexameric FliI ring (PDB: 2DPY) (Imada et al.,

497   2007) and the monomer FliJ (PDB: 3AJW) (Ibuki et al., 2011) with α, β and γ subunit of bovine F$_1$-

498   ATPase (PDB: 1E79) (Gibbons et al., 2000) (Fig. S9). The models are then docked into 3-D density

499   maps by using the function "fit in map" in UCSF Chimera (Pettersen et al., 2004) (Figure 5). FliN is

500   organized in doughnut-shaped tetramers (Paul and Blair, 2006). Together with a recent crystal

501   structure FliM$_M$-FliG$_{MC}$ complex from *Thermotoga maritima* (PDB: 4FHR) (Vartanian et al., 2012), the

502   FliN-FliM$_M$-FliG$_{MC}$ complexs fit well into the bulge density at the bottom of the C-ring (Figure 5G-I;

503   Video 1). As V111, V112, V113 (*E. coli*) are in the hydrophobic patch and interaction with FliH (Paul et

504   al., 2006), we speculate those three Valine facing towards the FliH link. Those three Valine correspond

505   to V128, V129 and V130 in *T. maritima* (Paul et al., 2006). As a result, when we fit the FliN tetramer

506   ring, we have V128, V129 and V130 (See Movie S2 shown in red) facing towards the FliH link.

507
508

19

REFERENCES:

Abrusci, P., Vergara-Irigaray, M., Johnson, S., Beeby, M.D., Hendrixson, D.R., Roversi, P., Friede, M.E., Deane, J.E., Jensen, G.J., Tang, C.M*., et al.* (2012). Architecture of the major component of the type III secretion system export apparatus. Nature Structural &Amp; Molecular Biology *20*, 99.

Abrusci, P., Vergara-Irigaray, M., Johnson, S., Beeby, M.D., Hendrixson, D.R., Roversi, P., Friede, M.E., Deane, J.E., Jensen, G.J., Tang, C.M*., et al.* (2013). Architecture of the major component of the type III secretion system export apparatus. Nature structural & molecular biology *20*, 99-104.

Agulleiro, J.I., and Fernandez, J.J. (2011). Fast tomographic reconstruction on multicore computers. Bioinformatics *27*, 582-583.

Bai, F., Morimoto, Y.V., Yoshimura, S.D., Hara, N., Kami-Ike, N., Namba, K., and Minamino, T. (2014). Assembly dynamics and the roles of FliI ATPase of the bacterial flagellar export apparatus. Scientific reports *4*, 6528.

Beeby, M., Ribardo, D.A., Brennan, C.A., Ruby, E.G., Jensen, G.J., and Hendrixson, D.R. (2016). Diverse high-torque bacterial flagellar motors assemble wider stator rings using a conserved protein scaffold. Proc Natl Acad Sci U S A *113*, E1917-1926.

Bestor, A., Stewart, P.E., Jewett, M.W., Sarkar, A., Tilly, K., and Rosa, P.A. (2010). Use of the Cre-lox recombination system to investigate the lp54 gene requirement in the infectious cycle of *Borrelia burgdorferi*. Infection and immunity *78*, 2397-2407.

Charon, N.W., Cockburn, A., Li, C., Liu, J., Miller, K.A., Miller, M.R., Motaleb, M.A., and Wolgemuth, C.W. (2012). The unique paradigm of spirochete motility and chemotaxis. Annu Rev Microbiol *66*, 349-370.

Charon, N.W., Goldstein, S.F., Marko, M., Hsieh, C., Gebhardt, L.L., Motaleb, M.A., Wolgemuth, C.W., Limberger, R.J., and Rowe, N. (2009). The flat-ribbon configuration of the periplasmic flagella of *Borrelia burgdorferi* and its relationship to motility and morphology. Journal of bacteriology *191*, 600-607.

Chen, S., Beeby, M., Murphy, G.E., Leadbetter, J.R., Hendrixson, D.R., Briegel, A., Li, Z., Shi, J., Tocheva, E.I., Muller, A*., et al.* (2011). Structural diversity of bacterial flagellar motors. The EMBO journal *30*, 2972-2981.

Claret, L., Calder, S.R., Higgins, M., and Hughes, C. (2003). Oligomerization and activation of the FliI ATPase central to bacterial flagellum assembly. Molecular microbiology *48*, 1349-1355.

539 Diepold, A., and Armitage, J.P. (2015). Type III secretion systems: the bacterial flagellum and the
540 injectisome. Philosophical transactions of the Royal Society of London Series B, Biological sciences
541 *370*.

542 Erhardt, M., Mertens, M.E., Fabiani, F.D., and Hughes, K.T. (2014). ATPase-independent type-III
543 protein secretion in *Salmonella enterica*. PLoS genetics *10*, e1004800.

544 Erhardt, M., Namba, K., and Hughes, K.T. (2010). Bacterial nanomachines: the flagellum and type III
545 injectisome. Cold Spring Harbor perspectives in biology *2*, a000299.

546 Fan, F., and Macnab, R.M. (1996). Enzymatic characterization of FliI. An ATPase involved in flagellar
547 assembly in *Salmonella typhimurium*. J Biol Chem *271*, 31981-31988.

548 Ferris, H.U., Furukawa, Y., Minamino, T., Kroetz, M.B., Kihara, M., Namba, K., and Macnab, R.M.
549 (2005). FlhB regulates ordered export of flagellar components via autocleavage mechanism. J Biol
550 Chem *280*, 41236-41242.

551 Fraser, G.M., Gonzalez-Pedrajo, B., Tame, J.R., and Macnab, R.M. (2003). Interactions of FliJ with
552 the *Salmonella* type III flagellar export apparatus. Journal of bacteriology *185*, 5546-5554.

553 Gibbons, C., Montgomery, M.G., Leslie, A.G., and Walker, J.E. (2000). The structure of the central
554 stalk in bovine F(1)-ATPase at 2.4 A resolution. Nat Struct Biol *7*, 1055-1061.

555 Gonzalez-Pedrajo, B., Fraser, G.M., Minamino, T., and Macnab, R.M. (2002). Molecular dissection of
556 Salmonella FliH, a regulator of the ATPase FliI and the type III flagellar protein export pathway.
557 Molecular microbiology *45*, 967-982.

558 Hu, B., Lara-Tejero, M., Kong, Q., Galan, J.E., and Liu, J. (2017). In Situ Molecular Architecture of the
559 Salmonella Type III Secretion Machine. Cell *168*, 1065-1074 e1010.

560 Hu, B., Morado, D.R., Margolin, W., Rohde, J.R., Arizmendi, O., Picking, W.L., Picking, W.D., and Liu,
561 J. (2015). Visualization of the type III secretion sorting platform of *Shigella flexneri*. Proc Natl Acad Sci
562 U S A *112*, 1047-1052.

563 Ibuki, T., Imada, K., Minamino, T., Kato, T., Miyata, T., and Namba, K. (2011). Common architecture
564 of the flagellar type III protein export apparatus and F- and V-type ATPases. Nature structural &
565 molecular biology *18*, 277-282.

566 Ibuki, T., Uchida, Y., Hironaka, Y., Namba, K., Imada, K., and Minamino, T. (2013). Interaction
567 between FliJ and FlhA, components of the bacterial flagellar type III export apparatus. Journal of
568 bacteriology *195*, 466-473.

569 Imada, K., Minamino, T., Tahara, A., and Namba, K. (2007). Structural similarity between the flagellar
570 type III ATPase FliI and F1-ATPase subunits. Proc Natl Acad Sci U S A *104*, 485-490.

571 Kawamoto, A., Morimoto, Y.V., Miyata, T., Minamino, T., Hughes, K.T., Kato, T., and Namba, K.
572 (2013). Common and distinct structural features of *Salmonella* injectisome and flagellar basal body.
573 Scientific reports *3*, 3369.

574 Kihara, M., Minamino, T., Yamaguchi, S., and Macnab, R.M. (2001). Intergenic Suppression between
575 the Flagellar MS Ring Protein FliF of Salmonella and FlhA, a Membrane Component of Its Export
576 Apparatus. Journal of bacteriology *183*, 1655-1662.

577 Kremer, J.R., Mastronarde, D.N., and McIntosh, J.R. (1996). Computer visualization of three-
578 dimensional image data using IMOD. Journal of structural biology *116*, 71-76.

579 Kubori, T., Shimamoto, N., Yamaguchi, S., Namba, K., and Aizawa, S. (1992). Morphological pathway
580 of flagellar assembly in *Salmonella typhimurium*. J Mol Biol *226*, 433-446.

581 Kuhlen, L., Abrusci, P., Johnson, S., Gault, J., Deme, J., Caesar, J., Dietsche, T., Mebrhatu, M.T.,
582 Ganief, T., Macek, B.*, et al.* (2018). Structure of the Core of the Type Three Secretion System Export
583 Apparatus. bioRxiv

584 Lambert, A., Picardeau, M., Haake, D.A., Sermswan, R.W., Srikram, A., Adler, B., and Murray, G.A.
585 (2012). FlaA proteins in Leptospira interrogans are essential for motility and virulence but are not
586 required for formation of the flagellum sheath. Infection and immunity *80*, 2019-2025.

587 Li, C., Xu, H., Zhang, K., and Liang, F.T. (2010). Inactivation of a putative flagellar motor switch
588 protein FliG1 prevents *Borrelia burgdorferi* from swimming in highly viscous media and blocks its
589 infectivity. Molecular microbiology *75*, 1563-1576.

590 Li, H., and Sourjik, V. (2011). Assembly and stability of flagellar motor in *Escherichia coli*. Molecular
591 microbiology *80*, 886-899.

592 Li, X., Mooney, P., Zheng, S., Booth, C.R., Braunfeld, M.B., Gubbens, S., Agard, D.A., and Cheng, Y.
593 (2013). Electron counting and beam-induced motion correction enable near-atomic-resolution single-
594 particle cryo-EM. Nature methods *10*, 584-590.

595 Lin, T., Gao, L., Zhao, X., Liu, J., and Norris, S.J. (2015). Mutations in the Borrelia burgdorferi
596 Flagellar Type III Secretion System Genes fliH and fliI Profoundly Affect Spirochete Flagellar
597 Assembly, Morphology, Motility, Structure, and Cell Division. mBio *6*.

598 Liu, J., Howell, J.K., Bradley, S.D., Zheng, Y., Zhou, Z.H., and Norris, S.J. (2010a). Cellular
599 architecture of *Treponema pallidum*: novel flagellum, periplasmic cone, and cell envelope as revealed
600 by cryo electron tomography. J Mol Biol *403*, 546-561.

601 Liu, J., Lin, T., Botkin, D.J., McCrum, E., Winkler, H., and Norris, S.J. (2009). Intact flagellar motor of
602 *Borrelia burgdorferi* revealed by cryo-electron tomography: evidence for stator ring curvature and
603 rotor/C-ring assembly flexion. Journal of bacteriology *191*, 5026-5036.

604 Liu, J., Wright, E.R., and Winkler, H. (2010b). 3D visualization of HIV virions by cryoelectron
605 tomography. Methods in enzymology *483*, 267-290.

606 Macnab, R.M. (2003). How bacteria assemble flagella. Annu Rev Microbiol *57*, 77-100.

607 McMurry, J.L., Murphy, J.W., and Gonzalez-Pedrajo, B. (2006). The FliN-FliH interaction mediates
608 localization of flagellar export ATPase FliI to the C ring complex. Biochemistry *45*, 11790-11798.

609 McMurry, J.L., Van Arnam, J.S., Kihara, M., and Macnab, R.M. (2004). Analysis of the cytoplasmic
610 domains of *Salmonella* FlhA and interactions with components of the flagellar export machinery.
611 Journal of bacteriology *186*, 7586-7592.

612 Miller, M.R., Miller, K.A., Bian, J., James, M.E., Zhang, S., Lynch, M.J., Callery, P.S., Hettick, J.M.,
613 Cockburn, A., Liu, J.*, et al.* (2016). Spirochaete flagella hook proteins self-catalyse a lysinoalanine
614 covalent crosslink for motility. Nature microbiology *1*, 16134.

615 Minamino, T., and Imada, K. (2015). The bacterial flagellar motor and its structural diversity. Trends
616 Microbiol *23*, 267-274.

617 Minamino, T., and Macnab, R.M. (2000). Domain structure of *Salmonella* FlhB, a flagellar export
618 component responsible for substrate specificity switching. Journal of bacteriology *182*, 4906-4914.

619 Minamino, T., Morimoto, Y.V., Hara, N., and Namba, K. (2011). An energy transduction mechanism
620 used in bacterial flagellar type III protein export. Nature communications *2*, 475.

621 Minamino, T., and Namba, K. (2008). Distinct roles of the FliI ATPase and proton motive force in
622 bacterial flagellar protein export. Nature *451*, 485-488.

623 Minamino, T., Shimada, M., Okabe, M., Saijo-Hamano, Y., Imada, K., Kihara, M., and Namba, K.
624 (2010). Role of the C-Terminal Cytoplasmic Domain of FlhA in Bacterial Flagellar Type III Protein
625 Export. Journal of bacteriology *192*, 1929-1936.

626 Minamino, T., Yoshimura, S.D., Morimoto, Y.V., Gonzalez-Pedrajo, B., Kami-Ike, N., and Namba, K.
627 (2009). Roles of the extreme N-terminal region of FliH for efficient localization of the FliH-FliI complex
628 to the bacterial flagellar type III export apparatus. Molecular microbiology *74*, 1471-1483.

629 Moon, K.H., Zhao, X.W., Manne, A., Wang, J.Y., Yu, Z., Liu, J., and Motaleb, M.A. (2016).
630 Spirochetes flagellar collar protein FlbB has astounding effects in orientation of periplasmic flagella,
631 bacterial shape, motility, and assembly of motors in Borrelia burgdorferi. Molecular microbiology *102*,
632 336-348.

633 Motaleb, M.A., Corum, L., Bono, J.L., Elias, A.F., Rosa, P., Samuels, D.S., and Charon, N.W. (2000).
634 *Borrelia burgdorferi* periplasmic flagella have both skeletal and motility functions. Proc Natl Acad Sci
635 U S A *97*, 10899-10904.

636 Motaleb, M.A., Liu, J., and Wooten, R.M. (2015). Spirochetal motility and chemotaxis in the natural
637 enzootic cycle and development of Lyme disease. Current opinion in microbiology *28*, 106-113.

638 Motaleb, M.A., Miller, M.R., Bakker, R.G., Li, C., and Charon, N.W. (2007). Isolation and
639 Characterization of Chemotaxis Mutants of the Lyme Disease Spirochete *Borrelia burgdorferi* Using
640 Allelic Exchange Mutagenesis, Flow Cytometry, and Cell Tracking. Methods Enzymol *422*, 419-437.

641 Motaleb, M.A., Pitzer, J.E., Sultan, S.Z., and Liu, J. (2011). A novel gene inactivation system reveals
642 altered periplasmic flagellar orientation in a *Borrelia burgdorferi fliL* mutant. Journal of bacteriology
643 *193*, 3324-3331.

644 Murphy, G.E., Leadbetter, J.R., and Jensen, G.J. (2006). In situ structure of the complete *Treponema*
645 *primitia* flagellar motor. Nature *442*, 1062-1064.

646 Paul, K., and Blair, D.F. (2006). Organization of FliN subunits in the flagellar motor of *Escherichia coli*.
647 Journal of bacteriology *188*, 2502-2511.

648 Paul, K., Erhardt, M., Hirano, T., Blair, D.F., and Hughes, K.T. (2008). Energy source of flagellar type
649 III secretion. Nature *451*, 489-492.

650 Paul, K., Harmon, J.G., and Blair, D.F. (2006). Mutational analysis of the flagellar rotor protein FliN:
651 identification of surfaces important for flagellar assembly and switching. Journal of bacteriology *188*,
652 5240-5248.

653 Pettersen, E.F., Goddard, T.D., Huang, C.C., Couch, G.S., Greenblatt, D.M., Meng, E.C., and Ferrin,
654 T.E. (2004). UCSF Chimera--a visualization system for exploratory research and analysis. Journal of
655 computational chemistry *25*, 1605-1612.

656 Phillips, J.C., Braun, R., Wang, W., Gumbart, J., Tajkhorshid, E., Villa, E., Chipot, C., Skeel, R.D.,
657 Kalé, L., and Schulten, K. (2005). Scalable molecular dynamics with NAMD. Journal of computational
658 chemistry *26*, 1781-1802.

659 Raddi, G., Morado, D.R., Yan, J., Haake, D.A., Yang, X.F., and Liu, J. (2012). Three-dimensional
660 structures of pathogenic and saprophytic *Leptospira* species revealed by cryo-electron tomography.
661 Journal of bacteriology *194*, 1299-1306.

662 Saijo-Hamano, Y., Imada, K., Minamino, T., Kihara, M., Shimada, M., Kitao, A., and Namba, K.
663 (2010). Structure of the cytoplasmic domain of FlhA and implication for flagellar type III protein export.
664 Molecular microbiology *76*, 260-268.

665   Sultan, S.Z., Manne, A., Stewart, P.E., Bestor, A., Rosa, P.A., Charon, N.W., and Motaleb, M.A.
666   (2013). Motility is crucial for the infectious life cycle of *Borrelia burgdorferi*. Infection and immunity *81*,
667   2012-2021.

668   Sultan, S.Z., Sekar, P., Zhao, X., Manne, A., Liu, J., Wooten, R.M., and Motaleb, M.A. (2015). Motor
669   rotation is essential for the formation of the periplasmic flagellar ribbon, cellular morphology, and
670   Borrelia burgdorferi persistence within Ixodes scapularis tick and murine hosts. Infection and immunity
671   *83*, 1765-1777.

672   Sze, C.W., Smith, A., Choi, Y.H., Yang, X., Pal, U., Yu, A., and Li, C. (2013). Study of the response
673   regulator Rrp1 reveals its regulatory role in chitobiose utilization and virulence of *Borrelia burgdorferi*.
674   Infection and immunity *81*, 1775-1787.

675   Vartanian, A.S., Paz, A., Fortgang, E.A., Abramson, J., and Dahlquist, F.W. (2012). Structure of
676   flagellar motor proteins in complex allows for insights into motor structure and switching. J Biol Chem
677   *287*, 35779-35783.

678   Wagner, S., Konigsmaier, L., Lara-Tejero, M., Lefebre, M., Marlovits, T.C., and Galan, J.E. (2010).
679   Organization and coordinated assembly of the type III secretion export apparatus. Proc Natl Acad Sci
680   U S A *107*, 17745-17750.

681   Ward, E., Renault, T.T., Kim, E.A., Erhardt, M., Hughes, K.T., and Blair, D.F. (2018). Type-III
682   secretion pore formed by flagellar protein FliP. Molecular Microbiology *107*, 94-103.

683   Winkler, H. (2007). 3D reconstruction and processing of volumetric data in cryo-electron tomography.
684   Journal of structural biology *157*, 126-137.

685   Winkler, H., Zhu, P., Liu, J., Ye, F., Roux, K.H., and Taylor, K.A. (2009). Tomographic subvolume
686   alignment and subvolume classification applied to myosin V and SIV envelope spikes. Journal of
687   structural biology *165*, 64-77.

688   Wunder, E.A., Jr., Figueira, C.P., Benaroudj, N., Hu, B., Tong, B.A., Trajtenberg, F., Liu, J., Reis,
689   M.G., Charon, N.W., Buschiazzo, A*., et al.* (2016). A novel flagellar sheath protein, FcpA, determines
690   filament coiling, translational motility and virulence for the Leptospira spirochete. Molecular
691   microbiology *101*, 457-470.

692   Zhao, X., Norris, S.J., and Liu, J. (2014). Molecular Architecture of the Bacterial Flagellar Motor in
693   Cells. Biochemistry *53*, 4323-4333.

694   Zhao, X., Zhang, K., Boquoi, T., Hu, B., Motaleb, M.A., Miller, K.A., James, M.E., Charon, N.W.,
695   Manson, M.D., Norris, S.J*., et al.* (2013). Cryoelectron tomography reveals the sequential assembly of
696   bacterial flagella in *Borrelia burgdorferi*. Proc Natl Acad Sci U S A *110*, 14390-14395.

697 Zhu, K., González-Pedrajo, B., and Macnab, R.M. (2002). Interactions among Membrane and Soluble
698 Components of the Flagellar Export Apparatus of Salmonella. Biochemistry *41*, 9516-9524.

699 Zhu, S., Nishikino, T., Hu, B., Kojima, S., Homma, M., and Liu, J. (2017). Molecular architecture of the
700 sheathed polar flagellum in Vibrio alginolyticus. Proc Natl Acad Sci U S A *114*, 10966-10971.

701
702

702 **Figures and Figure legends**

703
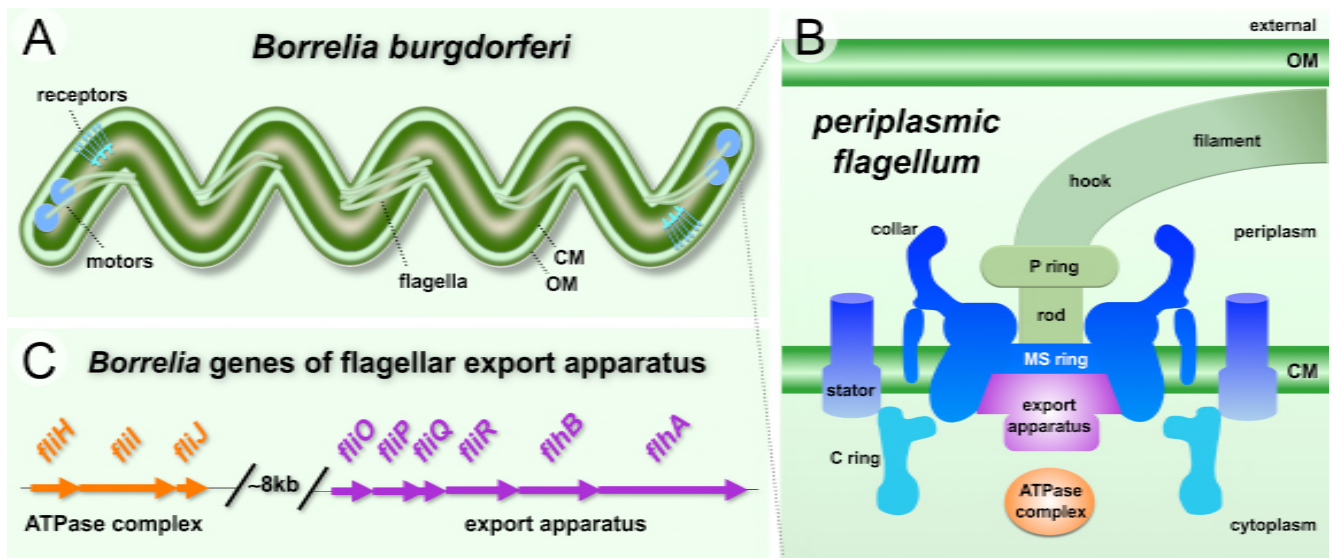
704

705

706 **Figure 1. Overview of the fT3SS in *B. burgdorferi*.** (A) Schematic model of *B. burgdorferi* and its

707 periplasmic flagella. (B) Model of the spirochete flagellar motor, showing the locations of major

708 components. The fT3SS is localized in the central region of the MS ring and the C-ring. (C) Gene

709 clusters encoding the fT3SS of *B. burgdorferi*. The six genes that encode membrane proteins are

710 marked in purple, while the genes that encode the cytoplasmic proteins are marked in orange. Note

711 that *fliJ* and *fliO* were also called *flbA* and *FliZ*, respectively.

712
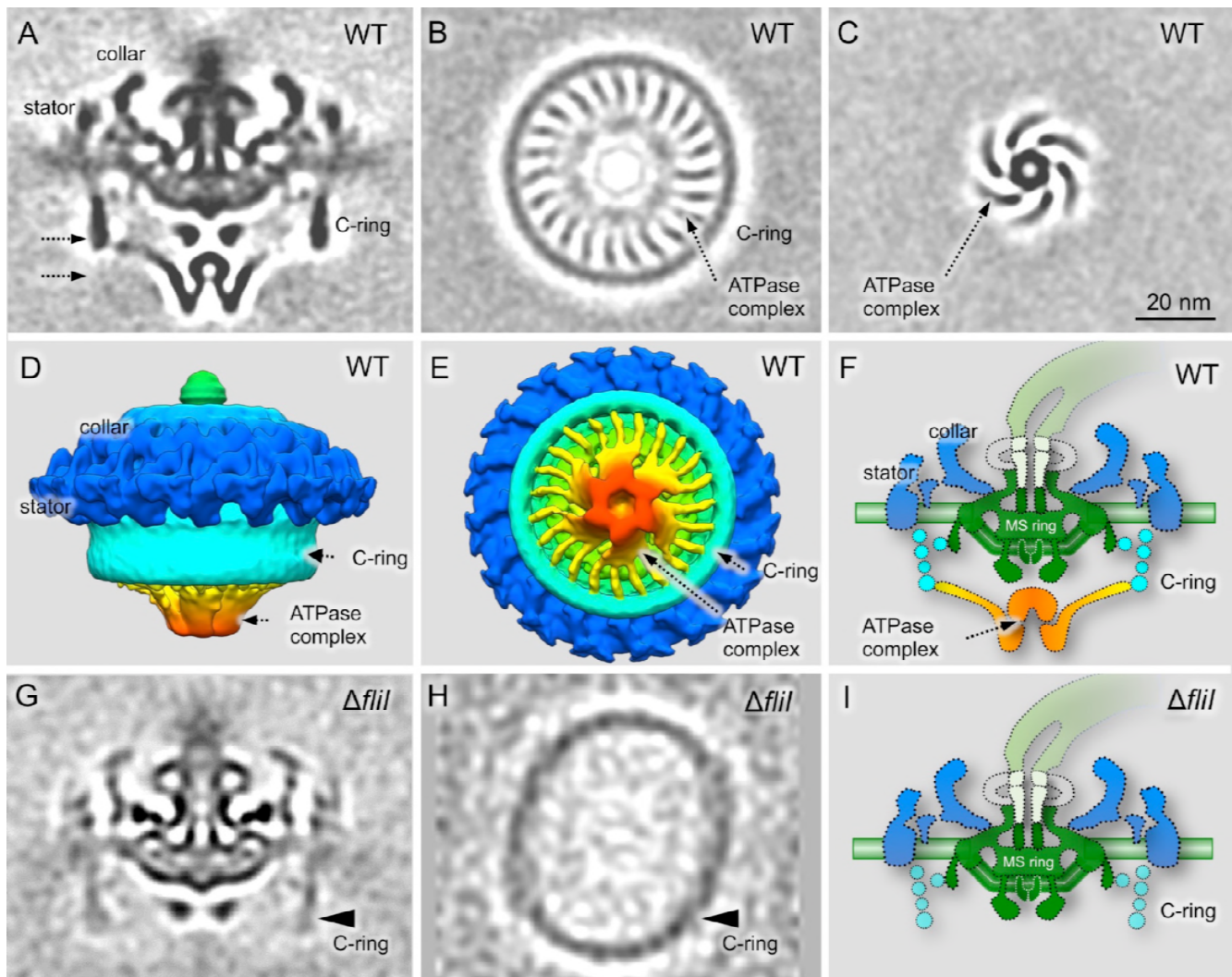
Figure 2. Cryo-ET reveals a novel ATPase complex structure in *B. burgdorferi*. (A) A central section of a flagellar motor structure from WT cells. The structure was generated by alignment of the ATPase ring complex region and classification of the linker region (see S1). (B) A cross section of the C-ring and linker region. 23 linkers connect the ATPase complex to the C-ring. (C) Another cross section shows the hexagonal "hub" structures. (D, E) Surface rendering of the WT flagellar motor structure from a side view and a bottom view, respectively. (F) A schematic model of the WT motor based on the averaged structure showed in (A). (G) A central section of the flagellar motor structure from a *fliI* mutant. The C-ring density from the *fliI* mutant is weak compared to that of the WT. (H) A cross section of the C-ring from the *fliI* mutant shows an ellipse-like structure, which is very different from the C-ring in the WT flagellar motor (B). (I) A schematic model of the flagellar motor structure in the *fliI* mutant.

28

726

727
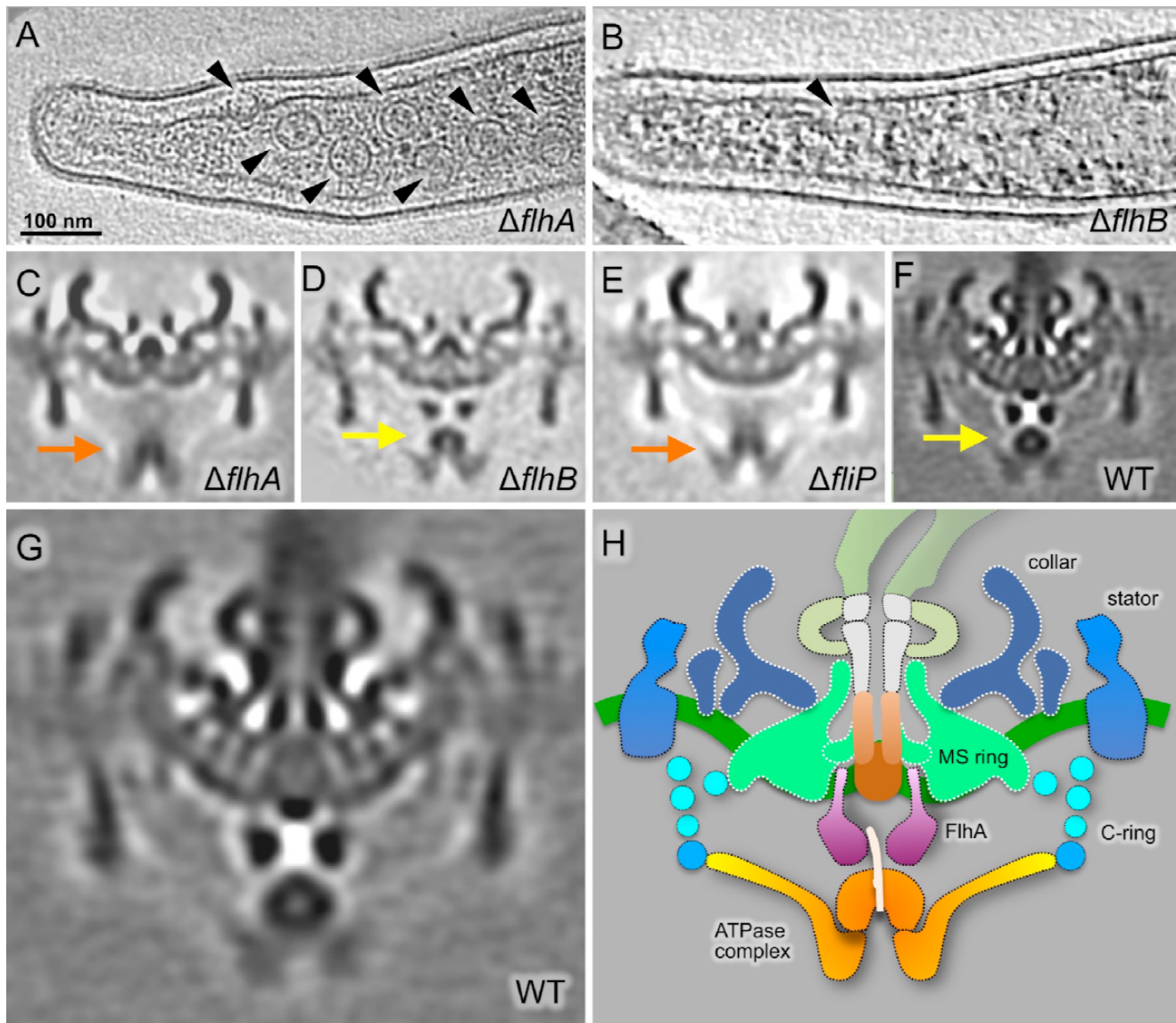
Figure 3. Characterization of the export apparatus. (A) Section of a tomogram from the Δ*flhA* mutant. Several motors can be seen in this representative cell tip (arrowheads). (B) Section of a tomogram from the Δ*flhB* mutant. Only one motor can be seen within this representative cell tip (arrowhead). Central sections of the average density maps of the flagellar motor are shown for (C) the Δ*flhA* mutant; (D) the Δ*flhB* mutant; (E) the Δ*fliP* mutant; and (F) WT. (G) Enlarged view of the average map of the flagellar motor from the WT. (H) Schematic model of the WT *B. burgdorferi* motor showing the proposed locations of fT3SS components in orange-yellow-purple.

735

736

29
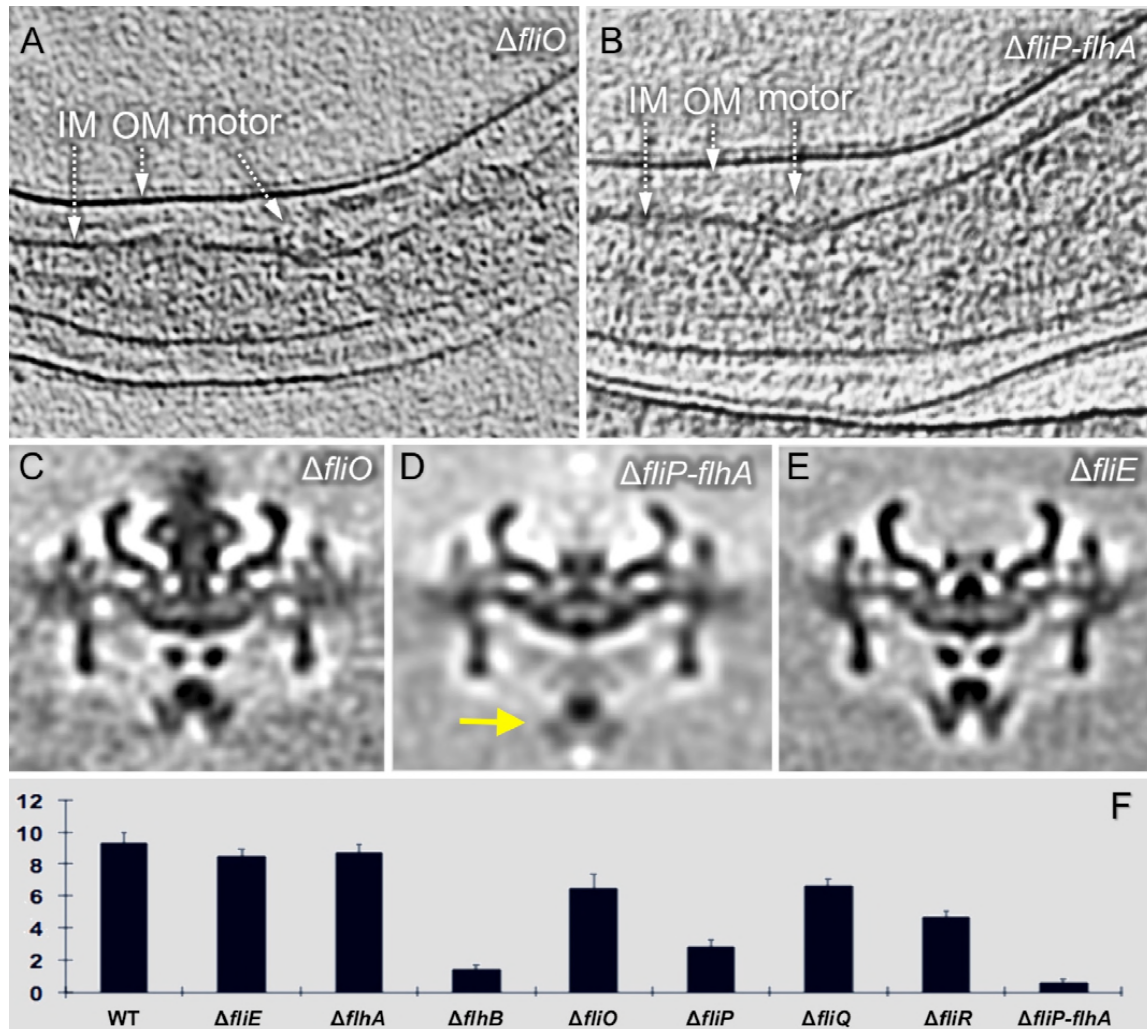
Figure 4. Structural characterization of the fT3SS in a Δ*fliO* mutant and a quintuple mutant. (A) Section of a tomogram of a Δ*fliO* mutant. (B) Section of a tomogram from a quintuple mutant in which the contiguous genes *fliP*, *fliQ*, *fliR*, *flhB*, and *flhA* were deleted. Central sections of average density maps are shown for the flagellar motors from (C) the Δ*FliO* mutant; (D) the quintuple mutant Δ*fliP-flhA*; and (E) the Δ*fliE* mutant, in which the export apparatus is intact while the rod is absent. (F) The number of motors per cell tip in the WT cells and the mutant cells is indicated.
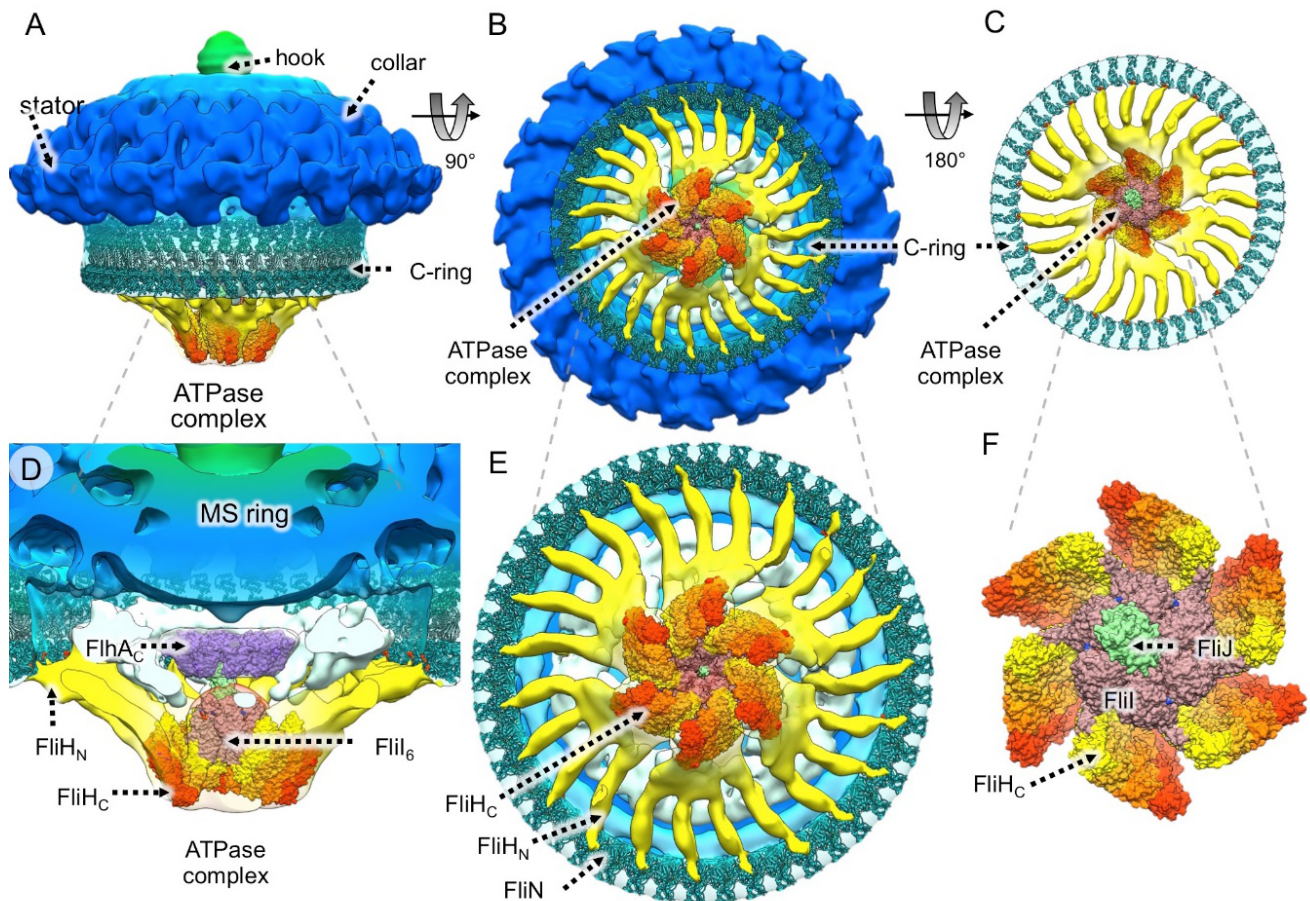
745
746 **Figure 5. Proposed molecular architecture of the fT3SS in the context of the flagellar motor.**

747 Crystallographic structures of FliH, FliI, and FliJ from other organisms (see Materials and Methods)

748 were positioned within the CryoET-derived density map of the large hexametric complex attached to

749 the C-ring protein FliN through FliH links. As there are the 23 FliH 'spokes' in the average structure,

750 we speculate there are 46 copies of the FliN tetramer, as well as 46 copies of $FliG_{MC}$-$FliM_M$ complex.

751 (A) A side view of the structure of the WT flagellar motor with the assembled C-ring (FliG, FliM and

752 FliN) and an ATPase complex (FliH, FliI and FliJ). (B) A bottom-up view of the C-ring and the ATPase

753 complex. (C) A top-down view of the assembled C-ring and the ATPase complex. (D) A sliced,

754 enlarged view of the ATPase complex and its interactions with FlhA and FliN. (E) An enlarged view

755 of the assembled C-ring and the ATPase complex. The hydrophobic surface (formed by Val-128, Val-

756 129 and Val-130) of FliN interacts with the FliH linker (yellow). (F) A close-up, top-down view of the

757 assembled ATPase complex in which six FliI monomers form the hub and at least 23 FliH dimers form

758 the spoke-like linkers.

31
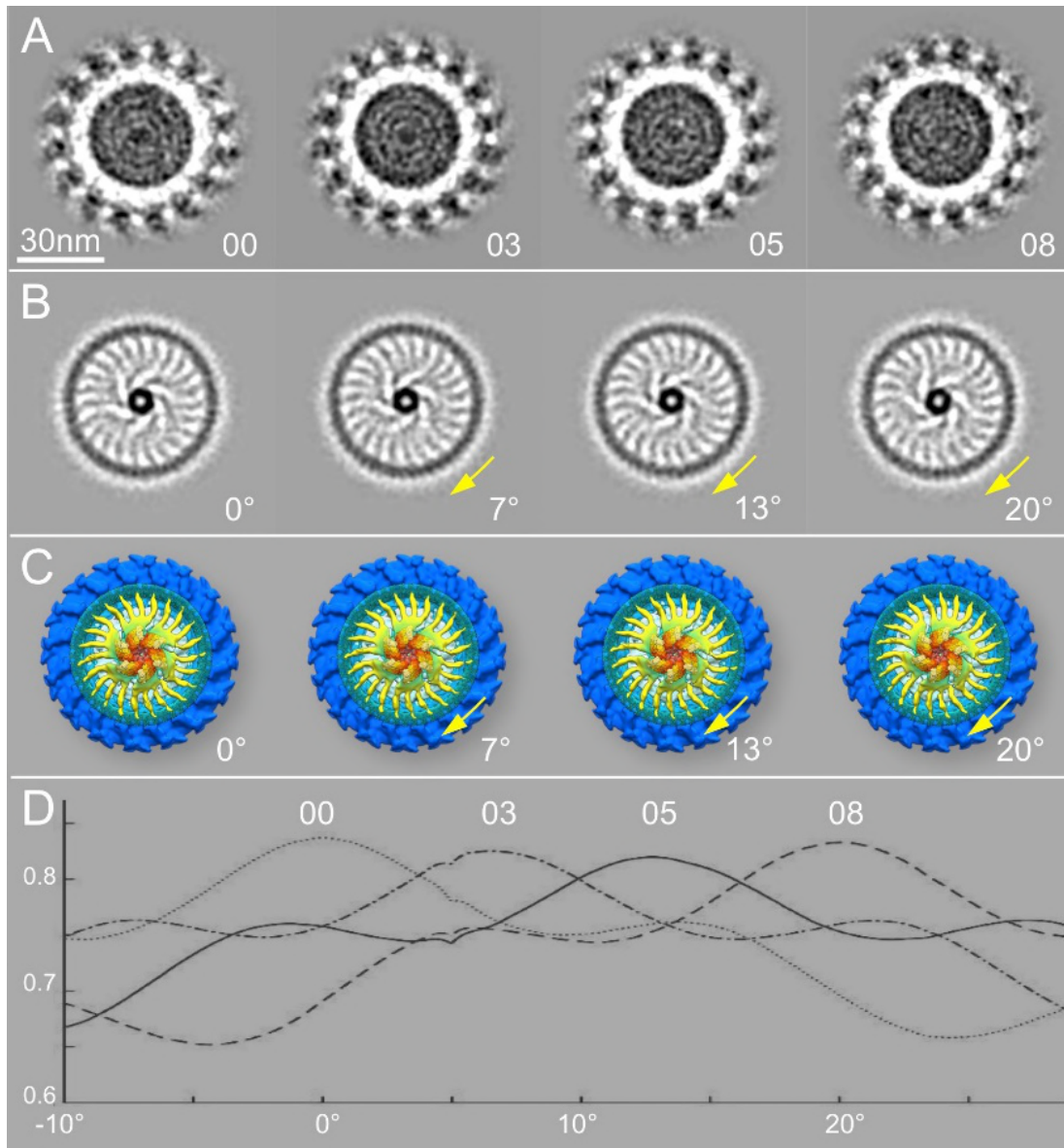
Figure 6. Variable conformations of the ATPase complex and the C-ring. (A) Sections of four class averages at the level of the 16 circumferential stator densities. Note that the stator densities exhibit very similar patterns. (B) Sections of the same class averages shown in panel A, but taken at the level of the FliI/FliH assembly and the C-ring. The sections show the ATPase complex in slightly different orientations. There are different rotations in classes 03, 05, and 08 relative to class 00. (C) Cytoplasmic views of the ATPase complexes from the four class averages, corresponding to the cross sections in panel B, respectively. (D) Cross correlation coefficient (CCC) between class averages. Note that the peak of the CCC for class 00 happens at 0° (without any in-plane rotation). The CCC peak for class 03 is located at ~7°, the CCC peak for class 05 at ~13°, and the CCC peak for class 08 at 20°.

32

769
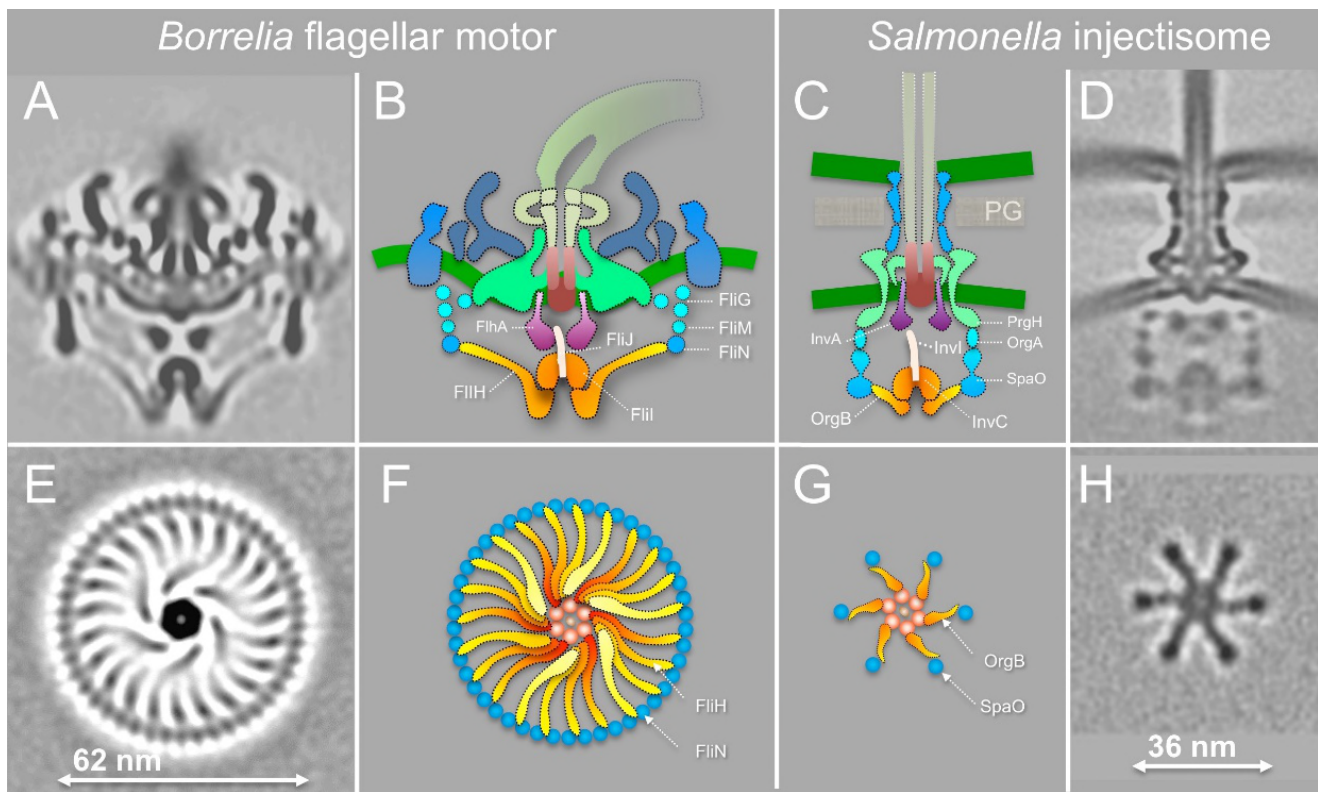
770

771 **Figure 7. Comparison of the fT3SS from *B. burgdorferi* and the vT3SS from *Salmonella*.** (A) A

772 central section from the WT *B. burgdorferi* motor. (B) The fT3SS in the spirochete motor consists of the

773 ATPase complex (orange) and the export apparatus (purple) underneath the MS-ring. (C, D) The

774 vT3SS from *Salmonella* injectisome is modeled in a similar color scheme (Hu et al., 2017; Hu et al.,

775 2015). The difference between the two T3SSs is striking in a comparison of the cross sections of their

776 ATPase complexes. Note that the C-ring from the *B. burgdorferi* motor is a continuous ring with ~46

777 copies of FliN tetramer. There are 23 visible FliH linkers (E, F). There are six pods in *Salmonella*

778 injectisome. Only six linkers of the FliH homolog OrgB connect the ATPase complex to the SpaO

779 molecules that compose the pod of the injectisome.

780

780
781 **SUPPLEMENTAL INFORMATION**
782
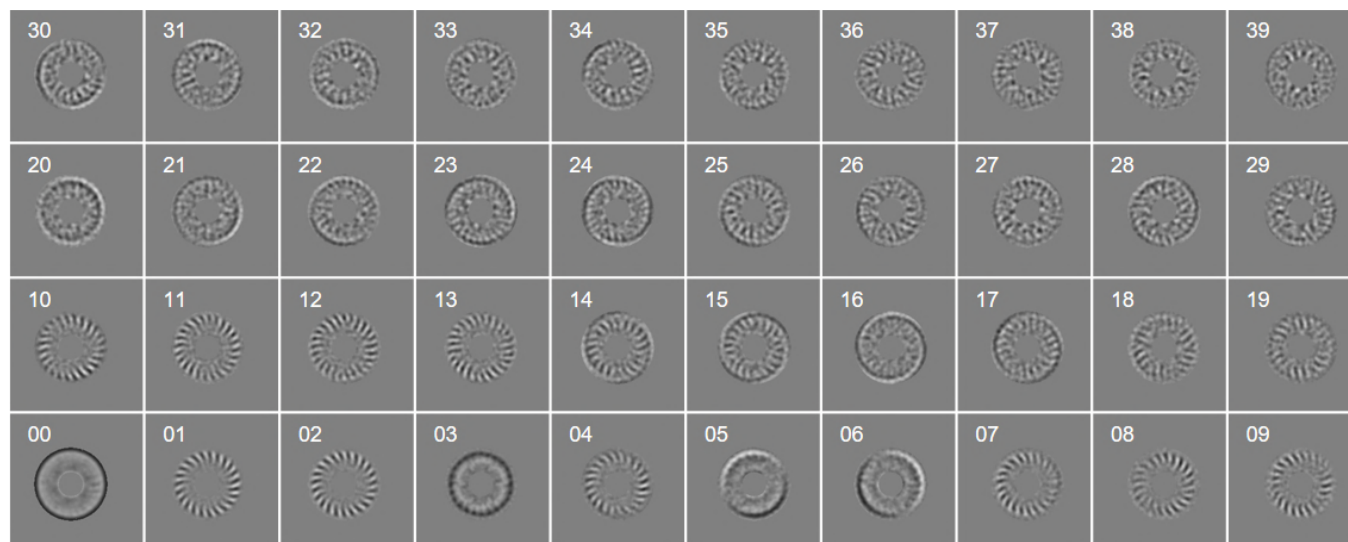
783
784
785 **Figure S1. Main eigen images for the classification on the spoke region.** The first 40 eigenimages of
786 the data set of ~30,000 sub-tomograms show different symmetry of the spoke region. Those sub-
787 tomograms were from c6 rotating of ~5000 motors along the axle, as the ATPase domain has the 6-
788 fold rotational symmetry. Eigenimages 01 and 02 exhibit 23-fold symmetry. Eigenimages 04 and 07
789 exhibit 22-fold symmetry. Eigenimages 08 and 09 exhibit 21-fold symmetry. Eigenimages 10 and 11
790 exhibit 24-fold symmetry.
791

34

A

WT

1	2	3	4
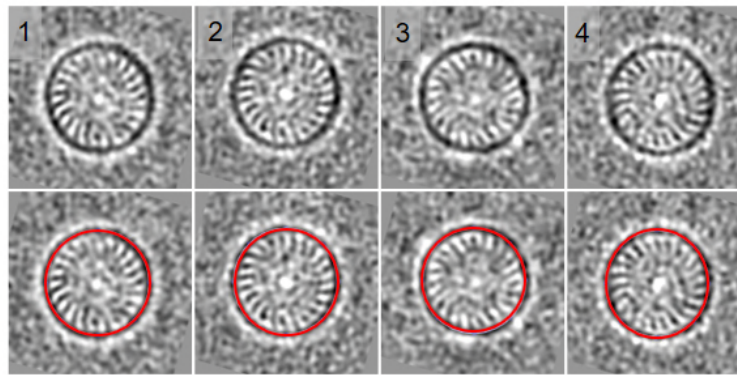
height/width ratio	1.005	1.014	1.019	1.048
% of motors	26.5%	25.5%	23.6%	24.4%

B

FliI

1	2	3	4
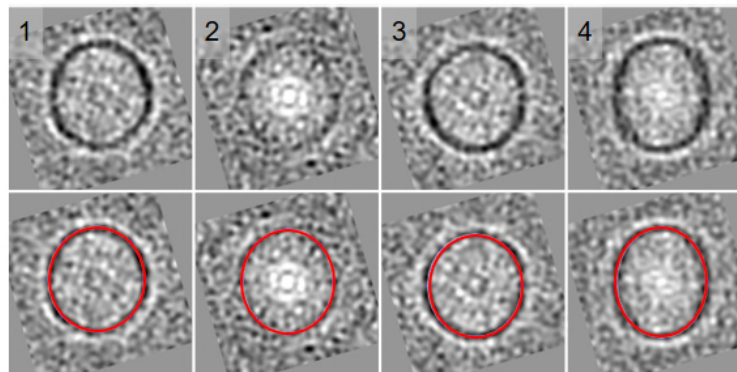
height/width ratio	1.075	1.129	1.088	1.206
% of motors	14.9%	49.9%	15.8%	19.3%

Figure S2. Comparison of flagellar C-ring in the WT and the Δ*fliI* mutant. *B. burgdorferi* flagellar motors from WT and *fliI* mutant were aligned and classified on the C-ring. The class averages were viewed in the cross section of the C-ring (sliced at position C as shown in Figure 2A). (A) Top: cross sections of 4 class averages from wild-type. Bottom: The red circle superimposed on the C-ring measures the height/width ratio of each class average. The ratio and the percentage of motors in each class are shown below the class averages. (B) Top: cross section of 4 class averages from the *fliI* mutant. Bottom: The red circle superimposed on the C-ring measures the height/width ratio of each class average. The ratio and the percentage of motors in each class are shown below the class averages.
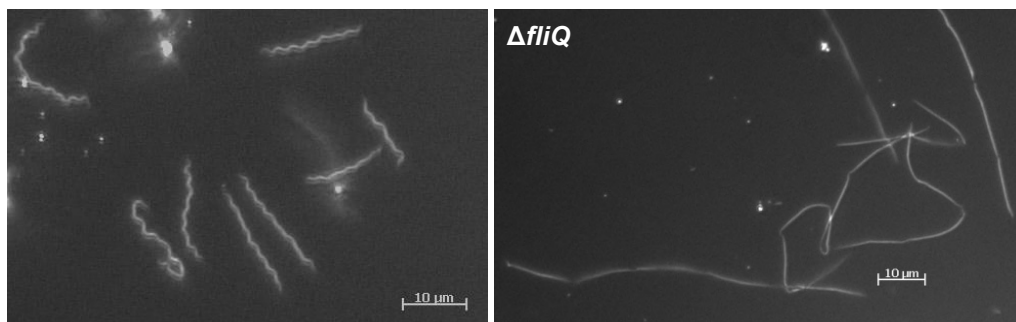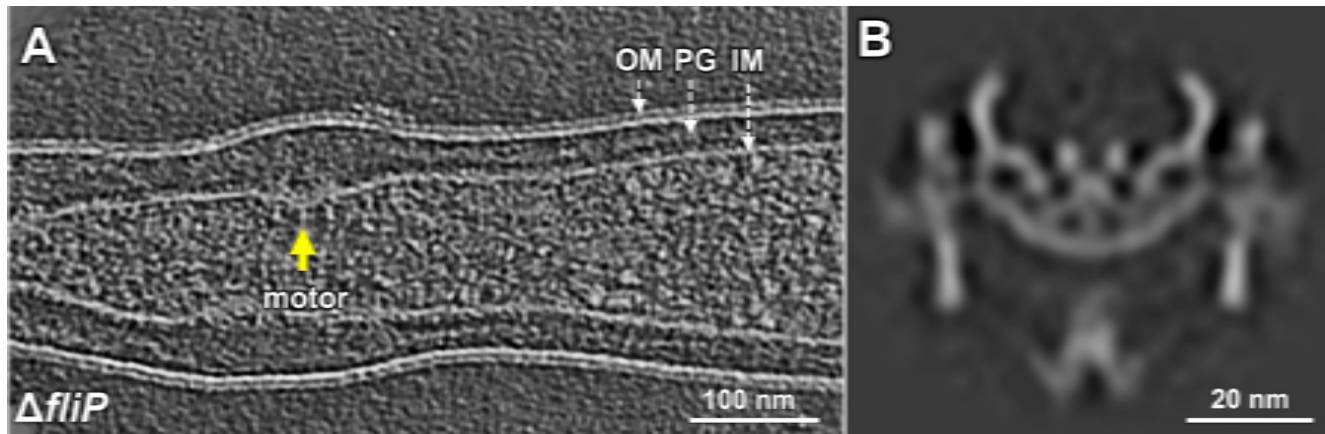
Figure S3. Dark-field images of the generated mutants. A representative dark-field image of motile, flat-wave wild-type (left), and a typical image of the rod-shaped, non-motile mutant (Δ*fliQ*).

35

809
810 **Figure S4. Structural characterization of the flagellar motor in *ΔfliP* cells.** (A) A section from a
811 tomogram of *ΔfliP* cells. One motor is highlighted in yellow arrow. (B) A central section of the
812 flagellar motor in *ΔfliP* cells.
813
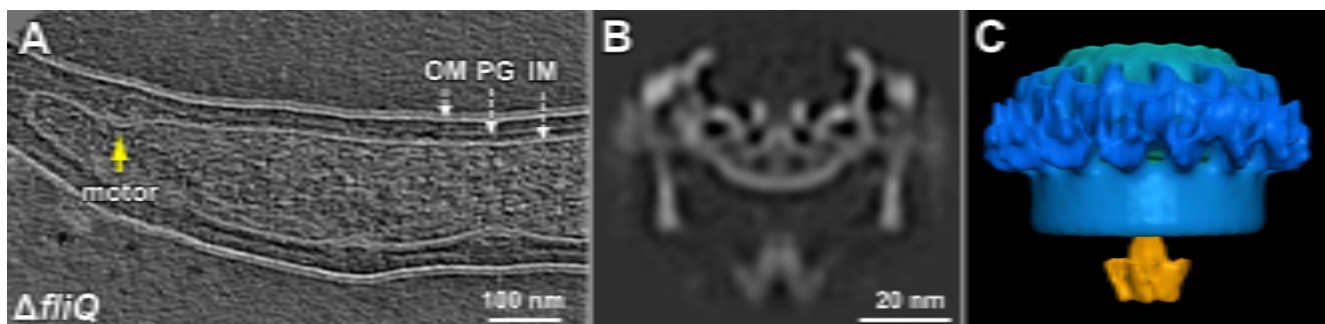
814
815 **Figure S5. Structural characterization of the flagellar motor in *ΔfliQ* cells**. (A) A section from a
816 tomogram of mutant *ΔfliQ* cells. One motor is shown in yellow arrow. (B, C) A central section and a
817 surface rendering of the sub-tomogram average of the flagellar motor in *ΔfliQ* cells, respectively.
818
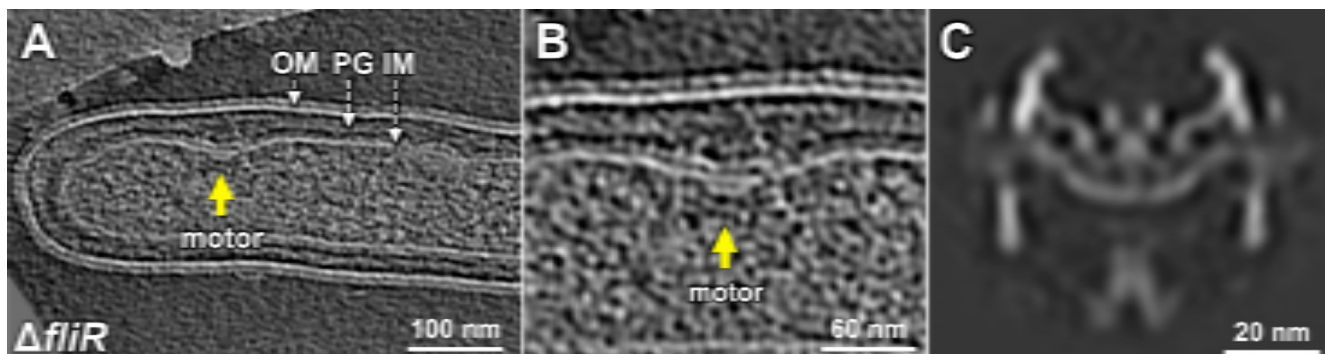
819
820 **Figure S6. Structural characterization of the flagellar motor in *ΔfliR* cells**. (A) A section from a
821 tomogram of *ΔfliR* cells. The yellow arrow indicates one motor. (B) A zoom-in view of the motor.
822 (C) A central section of the sub-tomogram average of the flagellar motor in *ΔfliR* cells.
823

36
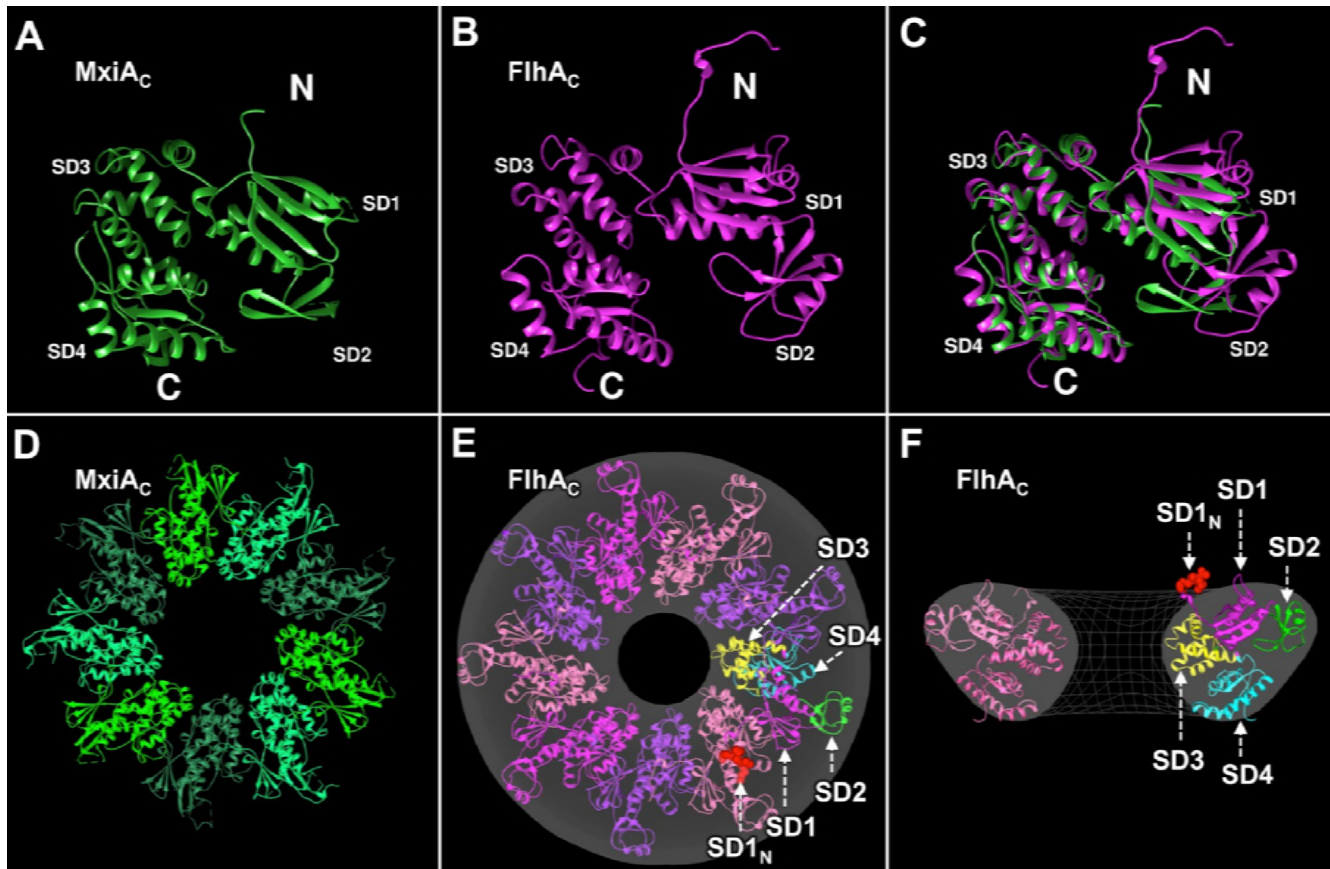
824
825
**Figure S7. Molecular model of FlhA_c nonameric ring**.
(A) Monomeric structure of the cytoplasmic domain (MxiA$_C$) of *Shigella flexneri* MxiA . There are four subdomains (SD1, SD2, SD3, and SD4). (B) Monomeric structure of the cytoplasmic domain (FlhA$_C$). (C) Two structures are aligned. (D) The crystal structure of the nonameric ring of MxiA$_C$. (E) A model of the nonameric ring of FlhA$_C$ was built based on the nonameric ring of MxiA$_C$. It fits well into the EM structure. Four subdomains are highlighted in different colors and the N-terminal five residues (SD1$_N$) are highlighted in red. (F) A central section of (E).
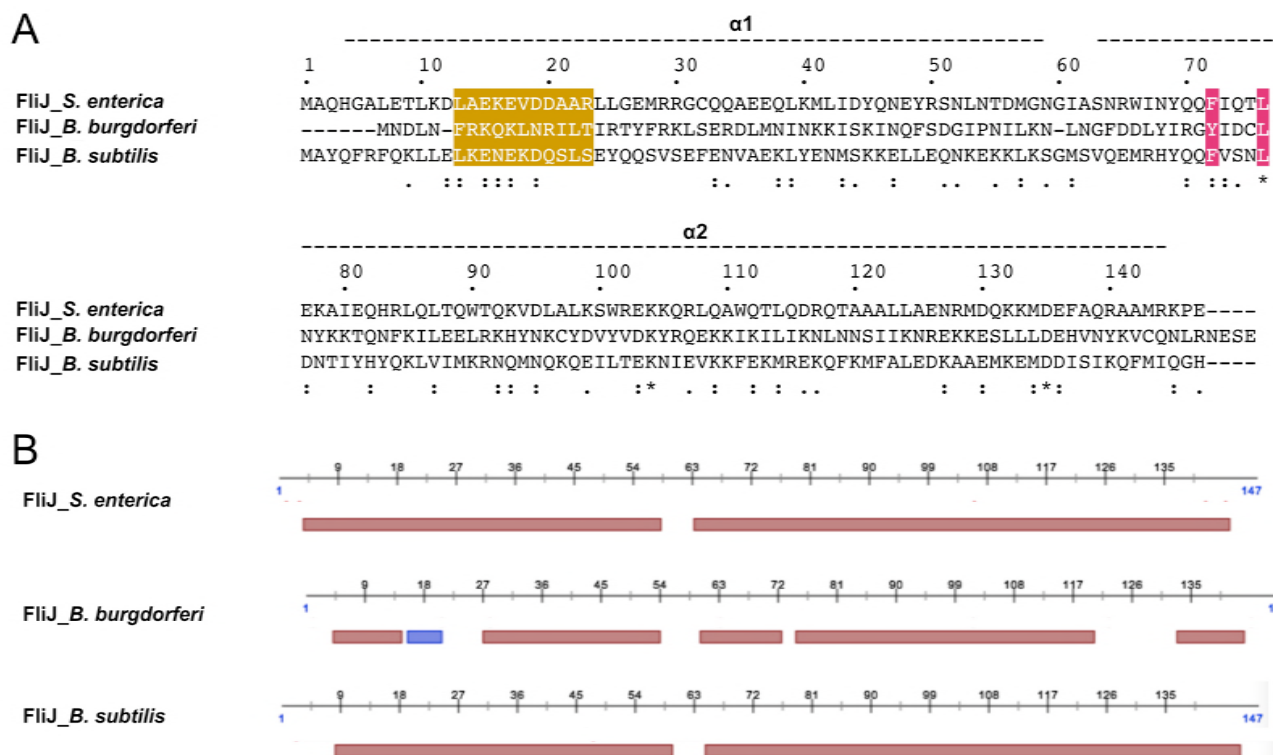
Figure S8. FliJ in *B. burgdorferi* is a homologue of FliJ in other bacteria.
(A) Sequences of *S. enterica* FliJ, *B. burgdorferi* FliJ and *B. subtilis* FliJ were aligned using CLUSTALW2. Asterisks under the sequences indicate the identical residues among the three bacteria; dots indicate similar residues. Residues 72 and 76 highlighted by red boxes with white letters were reported to interact with FlhA (Ibuki et al., 2013). Residues 13-24 highlighted by a yellow box with white letters were reported to interact with FliI (Minamino et al., 2011).
(B) Secondary structure prediction indicates that FliJ is mainly composed of alpha helices, similar to FliJ.

38
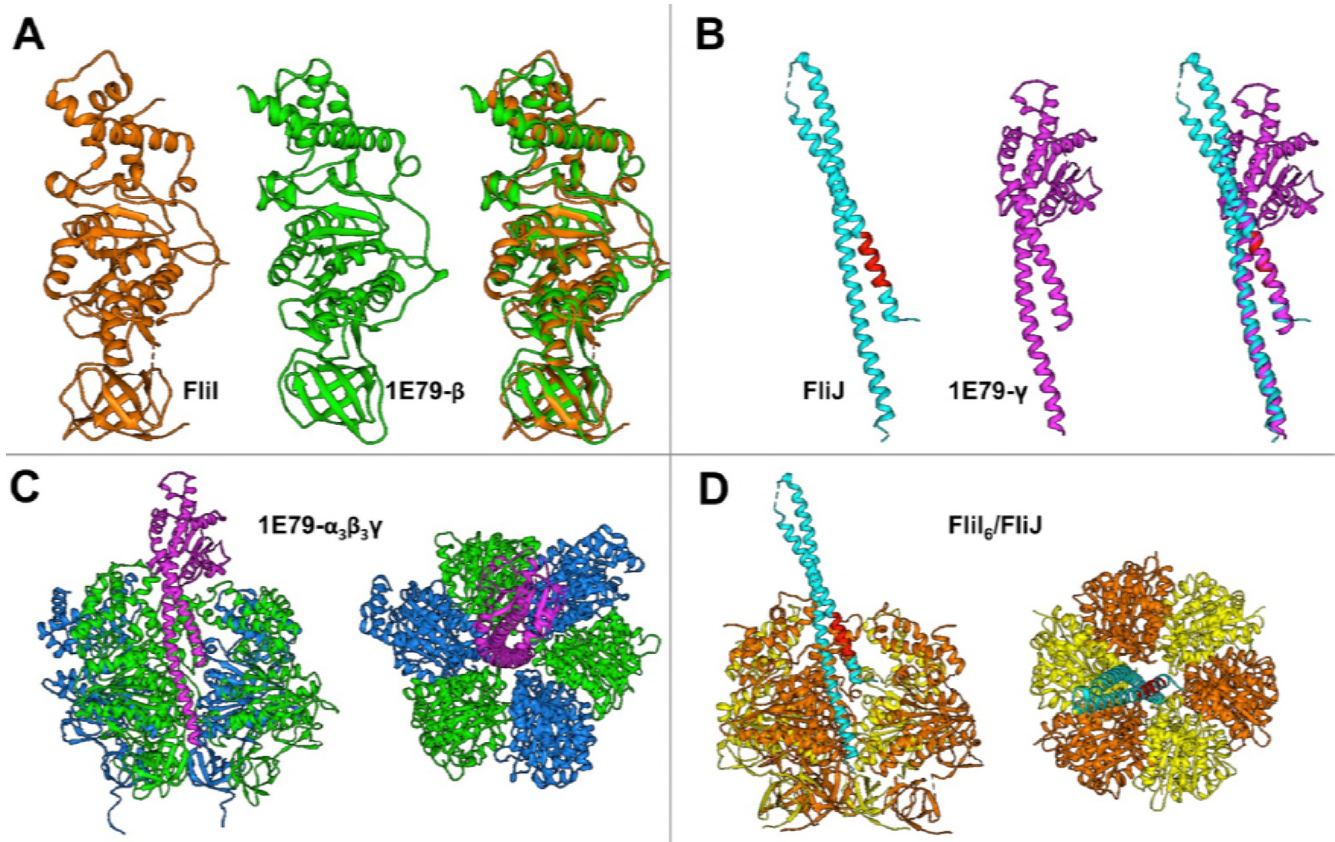
Figure S9. Molecular model of FliI/FliJ complex.

(A) The crystal structure of FliI from *S. enterica* is compared with the crystal structure of β subunit of F_1-ATPase.
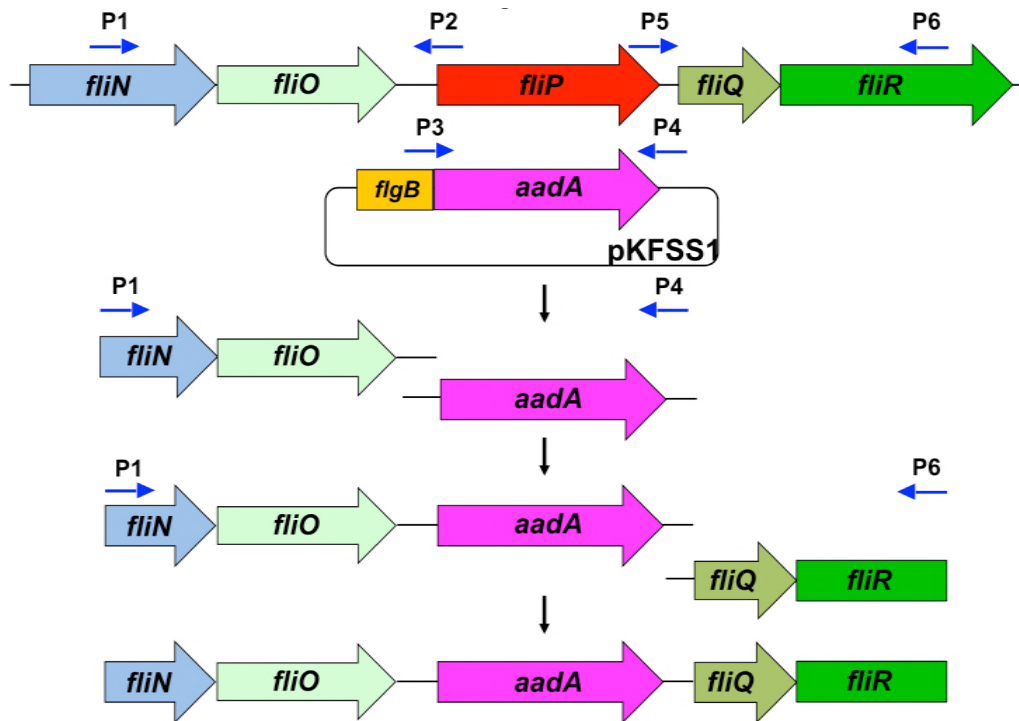
(B) The crystal structure of FliJ from *S. enterica* is compared with γ subunit of F_1-ATPase.

(C) The crystal structure of F_1-ATPase

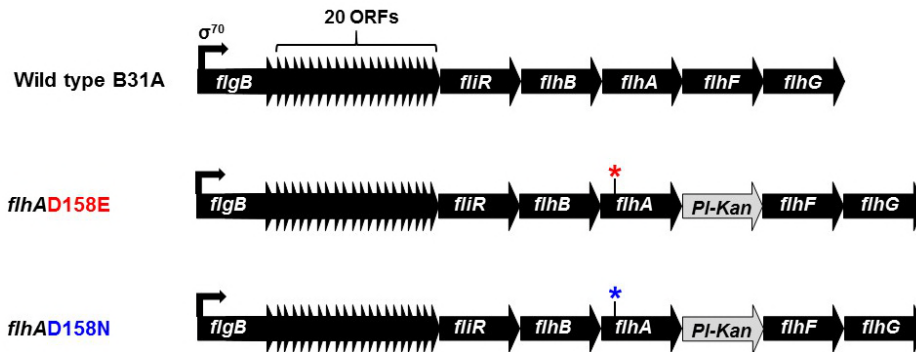(D) A homolog model of FliI/FliJ complex.

39

852 A

853
854 B

855
856 **Figure S10. (A) Construction of a non-polar Δ*fliP* mutant in *B. burgdorferi*.** Targeted inactivation of
857 *fliP* is achieved by homologous recombination using a streptomycin resistance gene (*aadA*) as a
858 marker. (B) Construction of point mutants in *B. burgdorferi flhA*. Point mutant *B. burgdorferi* clones
859 were created by mutating Asp to Glu or Asn (GAT to GAA or AAT, respectively) at position 158 of
860 FlhA. The point mutant *flhAD158E* exhibits non-motile phenotype whereas the *flhAD158N* cells show
861 reduced motility phenotype. These mutants' flagellar motors are similar to the *flhA*-deletion mutant
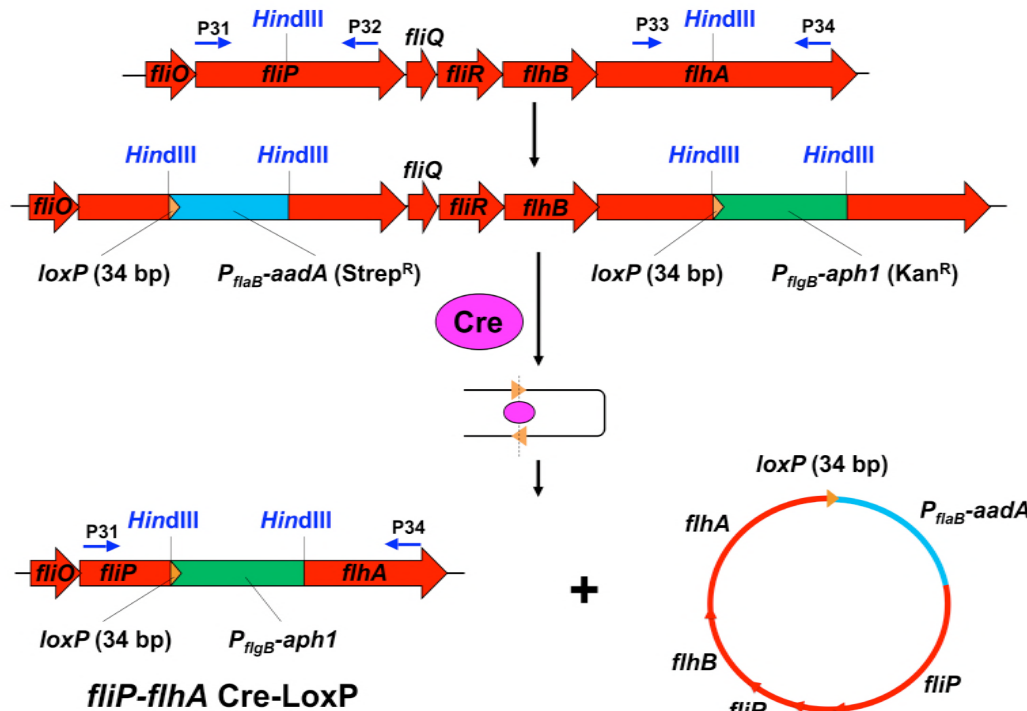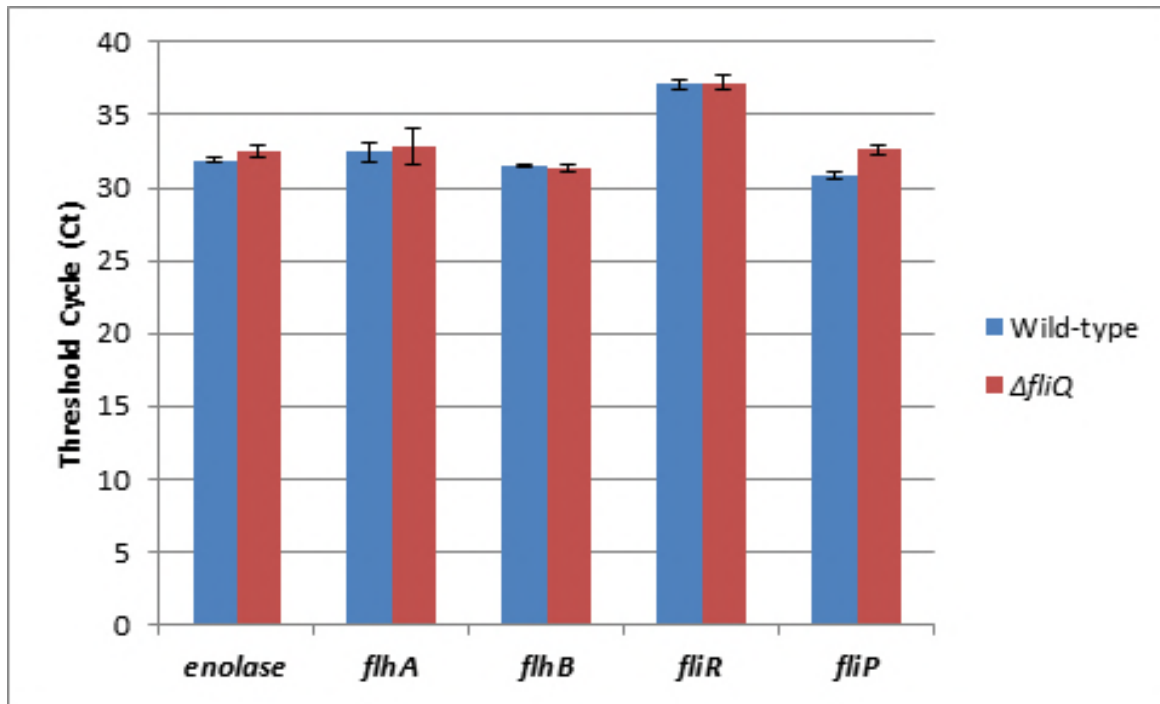862 Δ*flhA* (not shown).

40

863
864

865
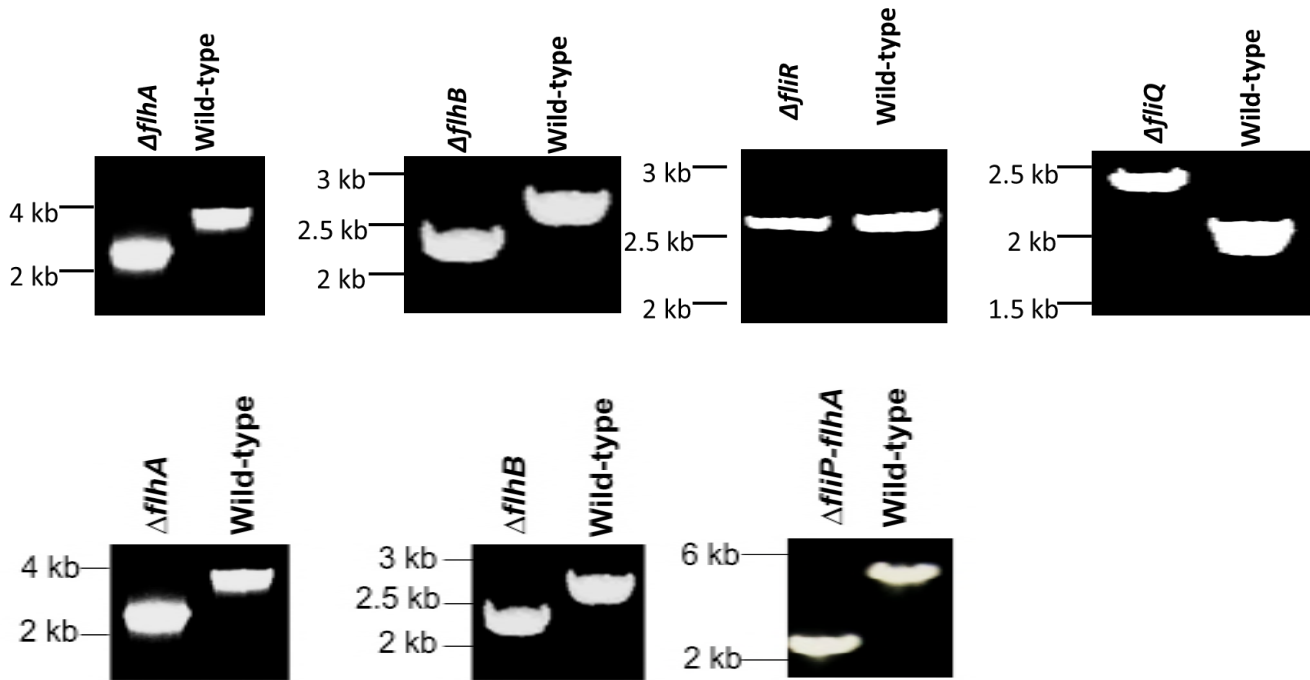
866
867 **Figure S11. PCR confirmation of the generated mutants**.
868 The PCR products are shown as expected.
869

870
871 **Figure S12. Construction of a quintuple *ΔfliP-flhA* mutant in *B. burgdorferi*.**
872 Deletion of the *fliP, fliQ, fliR, flhB, and flhA* genes is achieved by utilizing the Cre-*lox* recombination
873 system.

41

874
875 **Figure S13. Comparison of transcript levels between wild type and Δ*fliQ*.**
876 Transcript levels of *fliP* (which is located downstream of *fliQ*) and *fliR, flhB,* and *flhA* (located
877 upstream of *fliQ)* were measured using RNAs extracted from wild-type and Δ*fliQ* mutant cells. qRT-
878 PCR was performed using those RNA samples. *B. burgdorferi enolase* was used as a control. qRT-PCR
879 were carried out in triplicate and presented as the average of all three data sets (threshold cycle; Ct).
880
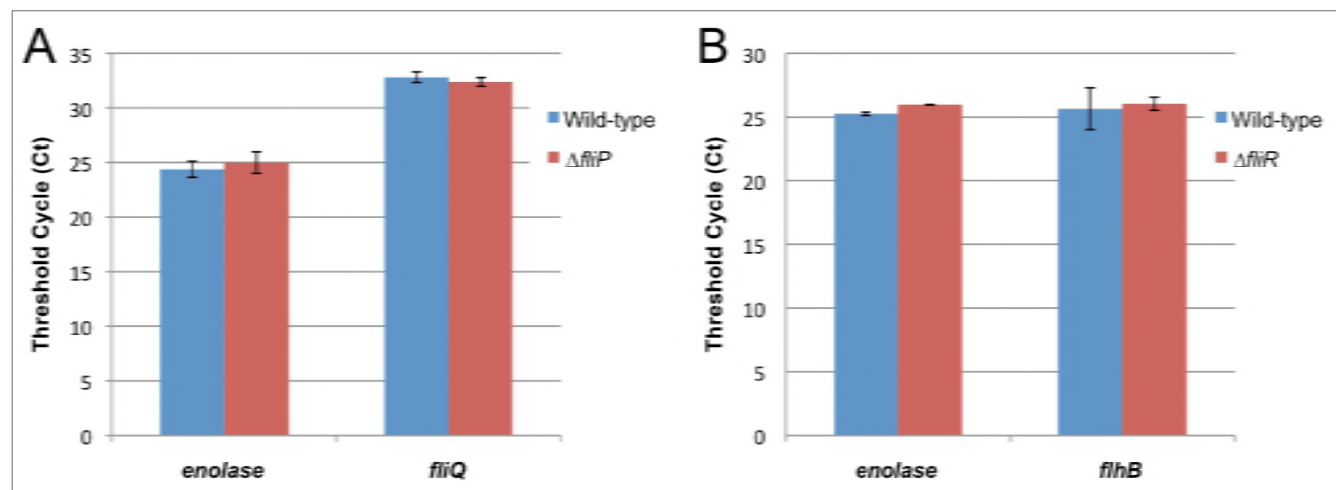
881
882 **Figure S14. Comparison of transcript levels between wild type, Δ*fliP*, and Δ*fliR*.**
883 (A) Transcript level of *fliQ* (which is located downstream of *fliP*) was measured using RNAs extracted
884 from wild-type and Δ*fliP* mutant cells. (B) Transcript level of *flhB* (which is located downstream of
885 *fliR*) was measured using RNAs extracted from wild-type and Δ*fliR* mutant cells. *B. burgdorferi enolase*
886 was used as a control. qRT-PCR were carried out in triplicate and presented as the average of all
887 three data sets (threshold cycle; Ct).
888
889
890
891
892

42

892
893   **Table S1. Sequence comparison of T3S proteins among *B. burgdorferi*, *S. enterica*, and *B. subtilis*.**
894

B. burgdoferi	*S. enterica*		*B. subtilis*	
	IDENTITY	**SIMILARITY**	**IDENTITY**	**SIMILARITY**
FlhA	35%	60%	40%	64%
FlhB	24%	46%	32%	58%
FliO (FliZ)	13%	28%	20%	36%
FliP	41%	61%	42%	64%
FliQ	40%	66%	43%	71%
FliR	19%	40%	24%	45%
FliH	13%	30%	20%	34%
FliI	41%	63%	44%	64%
FliJ (FlbA)	10%	17%	13%	34%

895
896

896
897 **Table S2. Mutants used in this study.**
898

B. burgdorferi	Gene	Gene product	Motility	Reference
Wild type	N/A	N/A	motile	Zhao. *et al.* (2013)
Δ*fliO*	BB0276	Flagellar biosynthesis protein FliO	motile	This study
Δ*flhA-flhB-fliP-fliQ-fliR*	N/A	N/A	nonmotile	This study
Δ*flhA*	BB0271	Flagellar biosynthesis protein FlhA	nonmotile	This study
flhA **D158E point mutant**	BB0271	Flagellar biosynthesis protein FlhA	nonmotile	This study
flhA **D158N point mutant**	BB0271	Flagellar biosynthesis protein FlhA	less motile	This study
Δ*flhB*	BB0272	Flagellar biosynthesis protein FlhB	nonmotile	This study
Δ*fliP*	BB0275	Flagellar biosynthesis protein FliP	nonmotile	This study
Δ*fliQ*	BB0274	Flagellar biosynthesis protein FliQ	nonmotile	This study
Δ*fliR*	BB0273	Flagellar biosynthesis protein FliR	nonmotile	This study

899

900
901   **Table S3. Primers used in this study.**
902

Primer Number	Sequence (5′ →3′)	Primer Name
P1	gagcttggaagaacagagcgc	FliP-P1-F
P2	ccctcataataaaccctctaaaatttttttaatc	Flip-P1-R
P3	gtttattatgagggaagcggtgatcgccg	FliP-KO-Strp-F
P4	ctagtattatttgccgactaccttggtg	Flip-KO-Strp-R
P5	caaataatactagtggtcttattaaaagt	FliP-P2-F
P6	gcttgacaaatcctgaatttc	FliP-P2-R
P7	gaaaattgaggcctcacttaagg	FliQ-P1-F
P8	ccctcatatataaccttacataaaacttttaataagacca	FliQ-P1-R
P9	ggttatatatgagggaagcggtgatcgccg	FliQ-KO-Strp-F
P10	ctaaaaatcttatttgccgactaccttggtg	FliQ-KO-Strp-R
P11	ggcaaataagatttttagtcaattgcaaaatg	FliQ-P2-F
P12	gcaagagaatctagtgaaagttc	FliQ-P2-R
P13	ggattttattaggcgtgctttatctcttc	FliR-P1-F
P14	cttccctcatttagtcataaattaaacattttgc	FliR-P1-R
P15	tgactaaatgagggaagcggtgatcgccgaag	FliR-KO-Strp-F
P16	ctagcattatttgccgactaccttggtgatc	FliR-KO-Strp-R
P17	gtcggcaaataatgctagttttttaaaattgttttc	FliR-P2-F
P18	ctgcttgaggaatagctactcttaaattg	FliR-P2-R
P19	gtactattgggatgaaattttg	FlhB-P1-F
P20	gcttccctcattattttaaaactctagaaaac	FlhB-P1-R
P21	gttttaaaataatgagggaagcggtgatcgccg	FlhB-KO-Strp-F
P22	ctttttagtattatttgccgactaccttgg	FlhB-KO-Strp-R
P23	cggcaaataatactaaaaagtttaattag	FlhB-P2-F
P24	caatcaagcctgtagacgttg	FlhB-P2-R
P25	gatctatcatggggtatgtcg	FlhA-P1-F
P26	cttccctcattagaacctctaattaaac	FlhA-P1-R
P27	gaggttctaatgagggaagcggtgatcgc	FlhA-KO-Strp-F
P28	ctactgttttttatttgccgactaccttgg	FlhA-KO-Strp-R
P29	cggcaaataaaaaacagtagaggttgaag	FlhA-P2-F
P30	gctccttcatctcagcaagc	FlhA-P2-R
P31	gaggcctcacttaaggataaac	FliP Cre F
P32	ggcaaagatatcatcacagg	FliP Cre R
P33	cttggtggtttgttagtggg	FlhA Cre F
P34	cgcttgagagaacaactgg	FlhA Cre R
P35	aagcttataacttcgtatagcatacat	pABA07 HindIII F
P36	aagcttttatttgccgactaccttgg	pABA07 HindIII R
P37	gctcaaatagttccccctacagaaatg	FliO-P1-F
P38	taactattattattcatttttagtttttaat	FliO-P1-R
P39	tgaataataatagttaaaagcaattttaaatg	FliO-KO-Kan-F
P40	atctatcttttagaaaaactcatcgagcatc	FliO-KO-Kan-R

P41	ttttctaaaagatagattaaaaaaattttag	FliO-P2-F
P42	ggcaaagatatcatcacaggggggcaac	FliO-P2-R
P43	cggtcggtttgatatttgttgttgc	FlhA qRT F
P44	gtcatcacaagcagtaatgtgggg	FlhA qRT R
P45	gaagaaccgaattacctactgacc	FlhB qRT F
P46	ggaagcttgatggcctgctc	FlhB qRT R
P47	cttttacaattttacctgtgttggttag	FliR qRT F
P48	cgcaaaagaaagcatattgtctaaagg	FliR qRT R
P49	gacagtattggtggttcagagatag	FliP qRT F
P50	ggagattgttgaagagataaagcacg	FliP qRT R
P51	tggagcgtacaaagccaacatt	Enolase qRT F
P52	tgaaaaacctctgctgccattc	Enolase qRT R

903
904
905
906 **Table S4. Cryo-ET and parameters used in this study.**
907

Genotype	Tomograms	Motors	Magnification	Pixel size (nm)	Resolution (Å)	Accession code
Wild type	780 (DDD)	7,242	15,400 (DDD)	0.25	30	EMD-5627
Δ*fliO*	108	546	31,000	0.57	43	EMD-6090
Δ*flhA-flhB-fliP-fliQ-fliR*	342	54	31,000	0.57	63	EMD-6094
Δ*flhA*	324	2,007	31,000	0.57	38	EMD-6088
Δ*flhB*	543	217	31,000	0.57	58	EMD-6089
Δ*fliP*	265	359	31,000	0.57	48	EMD-6091
Δ*fliQ*	255	1,403	31,000	0.57	41	EMD-6092
Δ*fliR*	229	830	31,000	0.57	41	EMD-6093

908
909
910

910
911
912
913   **Movie S1.** A class average shows the 16-fold symmetry at collar stator region, 23-fold symmetry of
914   the spoke-link links, and 6-fold symmetry of the ATPase complex. The left is the sideview with yellow
915   line slicing through, the right is the cross-slicing view corresponding to the yellow line.
916
917   **Movie S2.** Surface rendering of a rebuild map and atomic model fitting. The top part (collar, stator
918   and MS-ring) structure was from global average applied with 16-fold symmetry. The bottom part (C-
919   ring, spoke links and ATPase) structure was from a combine of class averages. Same in Fig. 5 and Fig.
920   6. In order to refine the bottom structure, the top part of those class averages were not aligned and do
921   not show the 16-fold symmetry. The hexagonal "hub" were segmented in chimera, and the FliI-FliH
922   atomic structure (pdb:5B0O) were initially fitted into the segmented density. However, as there is
923   extra density, and 3 to 4 links extend from the hub, we postulate there are more than one $FliH_2$. Three
924   more $FliH_2$ were placed next to the FliI-FliH atomic structure, and they were fitted into the density
925   using Molecular Dynamic Flexible Fitting in NAMD (Phillips et al., 2005). The movie here showed the
926   fitting process by morphing. The FliJ (pdb:3AJW) atomic model was inserted to the center of FliI
927   hexamer. The atomic structure of FlhA homolog MxiA (pdb: 4A5P) was fitted into the density by rigid
928   fitting in Chimera. The density of FlihA here was from refined alignment on spoke-like links and thus
929   did not show 9-fold symmetry. The atomic structure for FliG-FliM-FliN was a homology model based
930   on FliGMC-FliMM complex from *Thermotoga maritime* (Vartanian et al., 2012), with the hydrophobic
931   patch of FliN tetramer facing the links. There are 46 copies of FliG-FliM-FliN and they fit reasonably
932   in the C-ring density.
933
934   **Movie S3.** The symmetry of spoke-link mismatches with the symmetry of stators, suggesting the C-
935   ring and the ATPase rotate together relatively to the stators. The left are two cross section views from
936   stator (top) and link with the ATPase region (bottom), respectively. The right is the rebuild map
937   orientated correspondently to represent the mismatching. Although the figures were arranged as CW
938   rotation (CCW viewed from bottom), the rotation can be either CW or CCW, as they are WT motors
939   so the rotation orientation cannot be determined solely from cryo-ET image processing.
940
941
942